Czech Technical University in Prague
Faculty of Nuclear Sciences and Physical Engineering

Correlation femtoscopy at the STAR experiment

Výzkumný úkol

2016/2017
Bc. Lukáš Holub

Czech Technical University in Prague
Faculty of Nuclear Sciences and Physical Engineering

Correlation femtoscopy at the STAR experiment

Výzkumný úkol

Study field: Experimental Nuclear and Particle Physics
Department: Physics department
Supervisor: RNDr. Chaloupka Petr, Ph.D.

Prague, 2016/2017

Bc. Lukáš Holub

ČESKÉ VYSOKÉ UČENÍ TECHNICKÉ V PRAZE
FAKULTA JADERNÁ A FYZIKÁLNĚ INŽENÝRSKÁ
PRAHA 1 - STARÉ MĚSTO, BŘEHOVÁ 7 - PSČ 115 19

Katedra: fyziky **Akademický rok:** 2016/2017

VÝZKUMNÝ ÚKOL

Student: **Bc. Lukáš Holub**

Obor: Jaderné inženýrství

Vedoucí úkolu: RNDr. Petr Chaloupka, Ph.D

Název úkolu (česky/anglicky): **Korelační femtoskopie na experimentu STAR**

Correlation femtoscopy at the STAR experiment

Pokyny pro vypracování:

1) Ultra-relativistické srážky jader a kvarkgluonové plasma
2) Experiment STAR na urychlovači RHIC: subdetektory a softwarové vybavení
3) Teorie - dvoučásticová korelační femtoskopie
   i. Korelace identickýchčástic
   ii. Korelace neidentických částic a vliv dynamiky systému
4) Praktická část – femtoskopická analýza srážek Au+Au experimentu STAR
   i. Identifikace částic a rekonstrukce rozpadových vrcholů
   ii. Konstrukce neopravené korelační funkce
5) Shrnutí a závěr.

Práce bude vypracována v anglickém jazyce.

Součástí zadání výzkumného úkolu je jeho uložení na webové stránky katedry fyziky.

Literatura:

[1] K. Yagi et al., Quark-Gluon Plasma, Cambridge University Press 2005.
[2] M. A. Lisa et al, Ann.Rev.Nucl.Part.Sci. 55 (2005) 357-402.
[3] M. A. Lisa and S. Pratt, arXiv:0811.1352[nucl-ex]
[4] R. Lednicky et al., Phys.Part.Nucl. 40 (2009) 307-352
[5] R. Lednicky et al., Prog.Theor.Phys.Suppl. 193 (2012) 335-339
[6] S.V. Afanasiev et al., Physics Letters B 557 (2003) 157–166

Datum zadání: 31. 10. 2016

……..

Datum odevzdání: ***vedoucí katedry***

Acknowledgement:

I would like to thank RNDr. Petr Chaloupka, Ph.D. for his instructions, advice and language corrections.

Abstrakt

Z predpovedi Kvantovej Chromdynamiky (QCD) existuje fázový prechodu od stavu hadrónov do stavu neviazaných gluónov a kvarkov - Quark-Gluonová Plazma (QGP). Tento stav hmoty existuje pri extrémne vysokej teplote alebo hustote. Predpokladá sa, že až niekoľko milisekúnd po Veľkom Tresku, bol vesmír v plazmovom kvark-gluónovom stave.

V dnešnej dobe, vďaka technickému pokroku a vôli objavovať nové veci, ľudia dokážu experimentálne vytvoriť takýto stav hmoty v špeciálnych laboratóriách, ako je Brookhaven National Laboratory v New Yorku alebo CERN v Ženeve. Tieto laboratóriá majú urýchľovače, ktoré umožňujú vykonávať ultra-relativistické ťažké ionové kolízie, počas ktorých môže vzniknúť QGP. To nám dáva príležitosť študovať fázu hmoty v neviazanej oblasti QCD, formovanie hadrónovej hmoty a interakcie medzi hadrónmi.

V tejto práci prezentujeme predbežnú analýzu femtoskopických meraní korelácie dvoch pozitívne nabitých piónov pri malej relatívnej hybnosti pomocou STAR údajov z kolízií $p - Au$ pre $\sqrt{s_{NN}} = 200\,GeV$. Korelácia zahŕňa Bose-Einsteinovú a Coulombovú interakciu. Silná interakcia tu nie je zahrnutá pretože je zanedbateľná. Získané korelačné funkcie sú fitované Gauss a Levy funkciami. Tieto jednoduché fity nezahŕňajú oblasť malej relatívnej hybnosti $q \sim 0.05\,GeV/c$, pretože nie sú schopné opísať Coulombovú interakciu. Na záver sa ziskané výsledky porovnávajú s výsledkami z podobných experimentov.

Kľúčové slová: Kvantová Chromodynamika, Kvark-Gluonová Plazma, Korelačná Femtoskopia,

Abstract

According to prediction of the Quantum Chromodynamics (QCD), there is a phase transition from a state of hadrons to a state of deconfined gluons and quarks, this state of matter is called the Quark-Gluon Plasma (QGP). This state of matter exists at extremely high temperature or density. It is believed that up to a few milliseconds after the Big-Bang, the Universe was in a quark–gluon plasma state.

Nowadays, thanks to technical stride and volition to explore new things , people are able to create such a state of matter experimentally in the special laboratories such as Brookhaven National Laboratory in New York or CERN in Geneva. These laboratories have accelerators that allow to perform ultra-relativistic heavy ion collisions during which the QGP can be created. This gives us the opportunity to study a phase of matter in the deconfined region of QCD, the formation of hadronic matter and the interaction between hadrons.

In this work, we present a preliminary analysis of femtoscopy measurements of correlation of two positive charged pions at small relative momenta, using STAR data from $p - Au$ collisions at $\sqrt{s_{NN}} = 200\,GeV$. The correlation includes Bose-Einstein and Coulomb interaction. The strong interaction is not included here because it is negligible. Obtained correlation functions are fitted by Gauss and Levy functions. These simple fits do not include an area of small relative momentum $q \sim 0.05\,GeV/c$ because they are not able to describe Coulomb interaction. At the end of this work obtained results are compared with results from similar experiments.

Keywords: Quantum Chromodynamics, Quark-Gluon Plasma, Correlation Femtoscopy

Contents

List of Figures

Chapter 1

Introduction

Quantum Chromodynamic (QCD) is a type of quantum filed theory which describes the strong interaction between the fundamental particles quarks and gluons. These particles make up hadrons, which are splitted either into baryons (formed by three quarks such as the proton,neutron) or into mesons (formed by quark-antiquark pair such as the pion, kaon). Isolated quarks have not been observed so far.

In the prediction of QCD there is a possibility of transition from a state formed by hadrons to a state which is composed from deconfined quarks and gluons - the Quark-Gluon Plasma (QGP). It is believed that this state of matter was at the beginnig of the universe.

In present, QGP can be also created in laboratories and it can be studied. However this system exists only for a very short period of time with typical space-time extents on the order of $10^{-14}\,m$. Using the Correlation Femtoscopy one can obtain information about the space-time characteristics of the system at the moment of particle emission.

This work is a preliminary analysis of two positive pion femtoscopy for $p - Au$ collisions at $\sqrt{s_{NN}} = 200\,GeV$. It is divided into six chapters. In the first chapter we introduce a brief overview of the Standart Model, Quantum Chromodynamics and Quark-Gluon Plasma. In the second chapter one can find a description of the geometry and space-time evolution of the collision. At the and of this chapter some signatures of the QGP are given. The third chapter contains describtion of the STAR detector at RHIC. Theoretical backgrounds of femtoscopy is discussed in chapter four. Here, the derivation of the two-particle correlation function for identical particles as well as parametrization of the coordinate system are shown, then the main idea of the non-identical correlation femtoscopy is described and the ending of this chapter contains information about femtoscopy in the dynamical system. The used data set and applied selection criteria for construction of correlation functions are discussed in chapter five. The last chapter summarizes our results. Here, some correlation functions are created for several multiplicity and k_T bins. These functions are fitted by Gauss ane Levy

function and from these fits one obtains the HBT radii, λ parameter and levy (α) parameter. Subsequently, these results are compared with each other and with results from differents experiments.

Chapter 2

Quark-gluon plasma

2.1 Standart model

The following subsection is mostly cited from [33]
The whole Universe is made from a few basic building blocks called fundamental particles which are governed by four fundamental interactions. Our understanding of how these particles and three of the forces are related to each other is encapsulated in the Standart model of particle physics. Every piece of matter is made of fundamental particles. These particles are divided into three classes: fermions, gauge bosons and Higgs boson.

2.1.1 Fundamental particles

Fermions are particles with spin of 1/2 and respect the Pauli exclusion principle. These particles can be splitted into two groups called quarks and leptons. There are six particles in each group which are grouped into three generations.

The quarks are distinguished according their flavor as up (u), down (d), strange (s), charm (c), bottom (b) and top (t). Each quarks carries a fraction of the elementary charge (2/3 or $-1/3$) and one of the three colors (red, green, or blue). In nature the quarks have never been observed individually, but only inside bound colorless strongly interacting particles called hadrons which are divided into mesons and baryons. Mesons are bound states of quark-antiquark pairs while baryon are bound states of three quarks.

The leptons are also grouped into the three generations where each generation consists of one lepton and its corresponding neutrino, i.e. electron (e^-), electron neutrino (ν_e), muon (μ), muon neutrino (ν_μ), tau (τ), tau neutrino (ν_τ). Electron, muon and tau carry the elementary charge while corresponding neutrinos carry no charge. For every quark and lepton there is also a corresponding antiparticle, the particle with the same mass and opposite charge.

The gauge bosons are vector particles with a spin of 1 that carry any of the fundamental interactions of the nature. This class contains gluon (g), photon (γ), Z boson (Z) and W boson ($W^{\pm}$). The massless electricaly neutral photon is associated with the electromagnetic interaction. The gluons are mediators of the strong interaction while the massive ellectrically neutral Z bosons and electrically charged $W^{\pm}$ bosons mediate the weak interaction.

The Higgs boson (H) is the scalar particle which gives mass to other fundamental particles.

Following figure (Fig.2.1) shows the overview of all previously discussed fundamental particles and their properties.

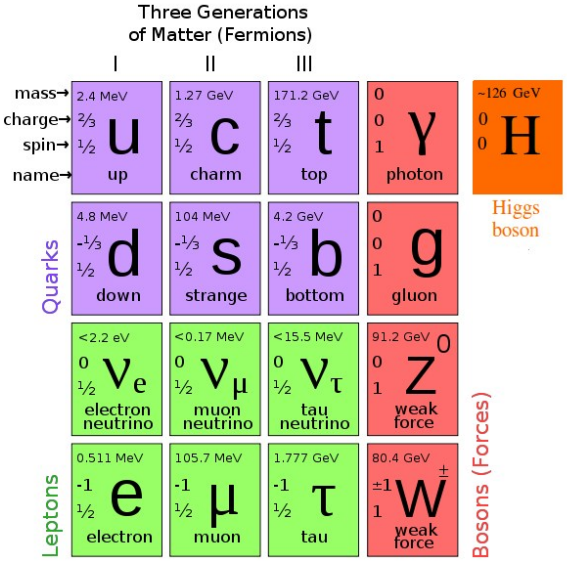

Figure 2.1: Fundamental particles in the Standart model and their properties. Taken from [13].

2.1.2 Fundamental interactions

The Standart model contains three fundamental interactions, namely strong, weak and electromagnetic. Each of these interactions is characterized by the corresponding gauge theory with a symmetry group and can be explained as exchange of mediators, the already discussed gauge bosons.

The mediator of the electromagnetic interaction is the photon and this interaction is described by the Quantum Electrodynamics. Since the photon has zero mass, the range of this force is infinity. On the other hand, the weak interaction is mediated by the massive $W^{\pm}$ and Z bosons, and therefore the range of this force is very short. These two forces can be united into the electroweak interaction.

The last fundamental force, which is contained in the Standart model, is the strong interaction with gluons as the mediators. Although the gluons are also massless particles like the photons, the strong interaction can reach up only units of fermi - $10^{-15}\,m$. This behavior is quite interesting and can be explained by the Quantum Chromodynamics (QCD), which will be discussed in detail in the following section.

Although the Standart model does not contain the gravitation force and its mediator, the graviton, and can not give an explanation of some phenomena, such as the non-zero mass of neutrino, it is one of the most widely accepted theoretical models in the particle physics.

Table 2.1 shows the summary of the fundamental interactions, their mediators, the range and the relative force with respect to the strong interaction.

Fundamental fource	Exchange boson	Mass (in MeV/c^2)	Expected range
Electromagnetic	Photon (γ)	0	∞
Weak	$W^{\pm}$, Z^0	$W^{\pm} = 80600$ $Z^0 = 93160$	$10^{-17} - 10^{-16}\,m$
Strong	Gluon (g)	0	$10^{-15}\,m$
Gravity	? Graviton ?	Not known to exist expected 0	∞

Table 2.1: Fundamental interactions in the Standard model and their properties.

2.2 Quantum chromodynamics

The Quantum Chromodynamics (QCD) is the gauge theory that describes the strong interaction, between quarks and gluons, with the SU(3) symmetry group. As mentioned above the mediatiors of this fundamental force are the massless gluons that carry the supplementary colour (anti-colour) charge. There are three different color charges (Red, Green and Blue) that create eight different gluons that occur in our world. The quarks interact with each other, with the possibility to change the relevant colour [10].

2.2.1 The Coupling constant and Asymptotic freedom

The strength of the strong interaction depends of a factor which is called the coupling constant α_s. The exchange of one gluon is proportional to a factor $g^2 = 4\pi\alpha_s$. In the figure below (Fig.2.2, right panel), each of the two vertices where the gluon and the quark get in touch contributes a factor of $g = \sqrt{4\pi\alpha_s}$. [2]

In QCD this constant α_s is not a constant at all because it decreases (increases) with increasing (decreasing) four momentum of the exchanged gluon (Q). The α_s lies

in the range $0.1 - 0.3$ at values of Q that can be probed experimentally, see in (Fig.2.2, left panel). The coupling constant α_s effectively depends on the four-momentum Q transferred in the interaction as [31]

$$\alpha_s(Q) = \frac{12\pi}{(33 - 2N_f) ln \frac{Q^2}{\Lambda_{QCD}}}$$

where N_f is the number of the of the quarks flavours and Λ_{QCD} is a scale parameter introduced by the renormallization process and is approximately equal to 200 MeV. [27]

Asymptotic freedom is one of the features of QCD that causes bonds between particles to become asymptotically weaker as momentum (energy) increases. This means that quarks interact weakly at high momenta (energies) and strongly at low momenta (energies), preventing of unbinding of baryons or mesons.

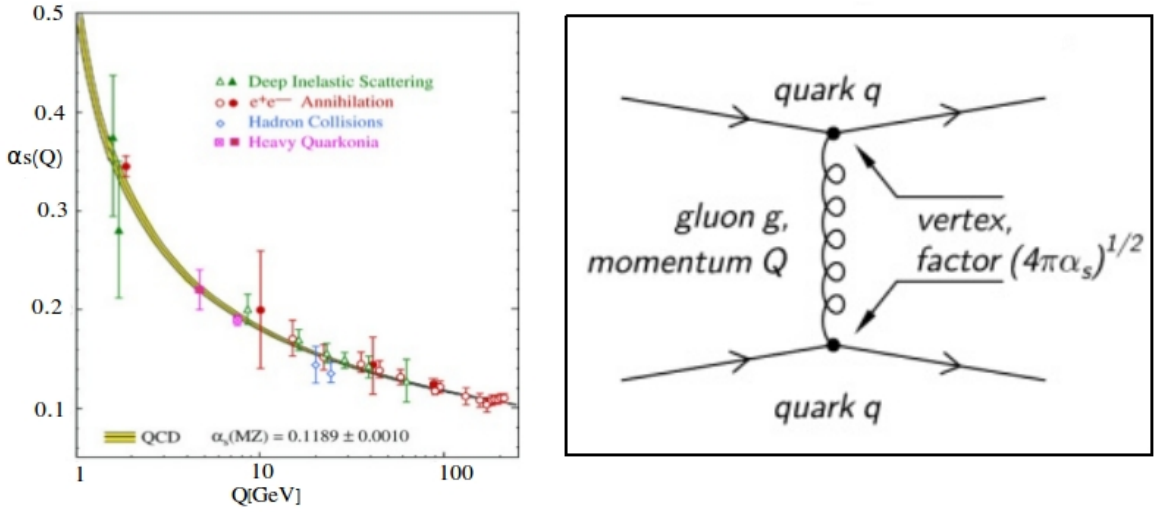

Figure 2.2: **Left)** It shows a compilation of the values for α_s, derived from many different experiments, and for different momenta Q of the exchanged gluons. Taken from [6]. **Right)** Two quarks exchange a gluon with momentum Q, and depending on the colour charge of the quarks, this exchange results in an attraction or a repulsion between both quarks. Taken from [2].

For comparison, in quantum electrodynamics (QED) the coupling constant, better known as *fine structure constant*, is a pure number, without dimensions of length or mass, independent of the momentum of the photon that is exchanged and has the value $\alpha = e^2/4\pi \approx 1/137$. This value is about 50 times smaller than in the case of coupling constant in QCD. That is why the strong interactions are *strong*.[2]

2.2.2 Color confinement

In the following idea one can understands the main idea of the color confinement.

Suppose, for example, we have a quark-antiquakr pair which is in a color singlet state. One may try to separate the quark from the antiquark by pulling them apart. The interaction between the quarks gets stronger as the distance between them gets arger, similar to what happens in the spring. In fact, when a spring is stretched beyond the elastic limit, it breaks to produce two springs. In the case of the quark pair, a new quark-antiquark pair will be created when pulled beyond certain distance. Part of the stretching energy goes into the creation of the new pair, and as a consequence, one cannot have quarks as free particles, see in (Fig.2.3, right panel).[1]

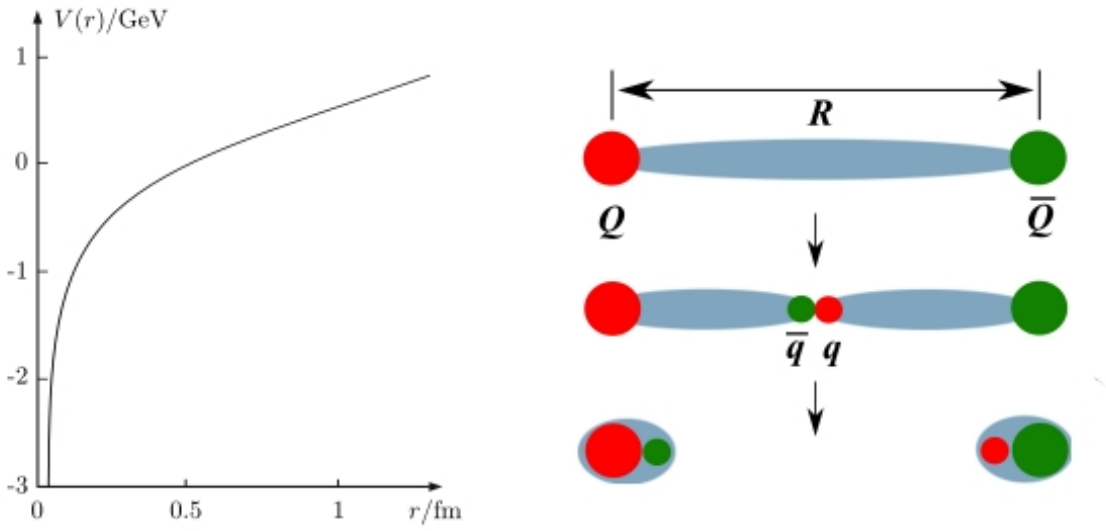

Figure 2.3: **Left)** The potencial between quark-antiquark pair in case of no light quarks in the QCD vacuum. **Right)** The QCD string spanned between the static quark-antiquark pair breaks due to light light quark-antiquark pair creation. Taken from [22]

The above discussion was only for imagination. However, to understand what really happens, one must make very difficult calculations in QCD. It can be shown that the effective quark-antiquark potential is well approximated by Cornell potential, see in (Fig.2.3, left panel)

$$V(r) = -\frac{4\alpha_s}{3r} + kr$$

where k is the string tensor that represents the strength of the quark confinement, r is the distance between quarks and α_s is the coupling constant.

The first term of the potential is well known Coulomb potential that depends on the factor $1/r$. The second term, a string potential, is more interesting because this term causes the fact that quarks can not never be seen in isolation under normal conditions.

2.3 Quark-gluon plasma

There are many questions in QCD phenomenology but one of the most important and interesting is what the properties are at the extreme densities and temperatures where the quarks and gluons are in a deconfined state [10]. Such a state of matter is known as the Quark Gluon Plasma (QGP). As mentioned above, under normal densities and temperatures the matter is in the well known confined hadronic state. However, everything changes when temperature and density of the system are extremely high. At these extreme values the QCD predicts a phase transition from hadronic state to the QGP. This phase transition can be seen in (Fig.2.4).

According to lattice QCD calculations the critical temperature of the phase transition is around $T_c \approx 170\,MeV$. At this temperature the energy density is $\epsilon_c \sim 1\,GeV/fm^3$, we expect to achieve the asymptotic freedom regime [10]. The QGP can be also established during the adiabatic compression of the nuclear matter at the temperature $T \approx 0\,MeV$. Since it is believed that the system can reach such a high baryon chemical density μ_B, where the binding between the quarks will be broken up and the QGP will be formed. In the (Fig.2.5) is shown a phase diagram of QCD.

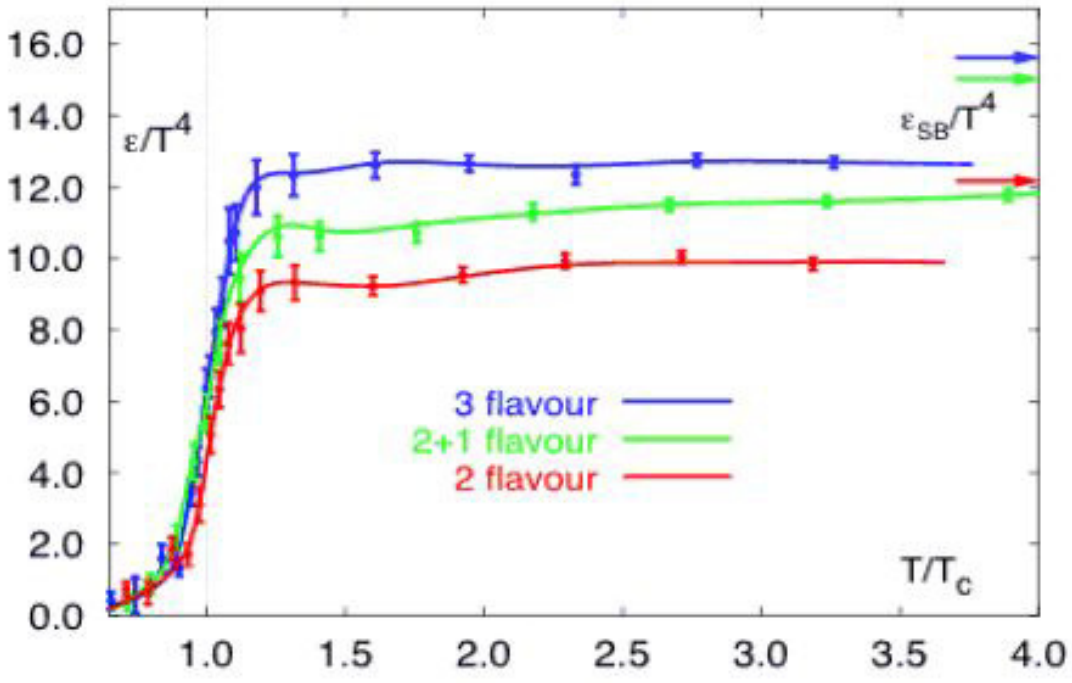

Figure 2.4: The energy density divided by the 4rth power of the temperature, computed on the lattice with different number of sea flavours, shows a marked rise near the critical temperature. The arrows on top show the limit for a perfect Bose gas. Taken from [17].

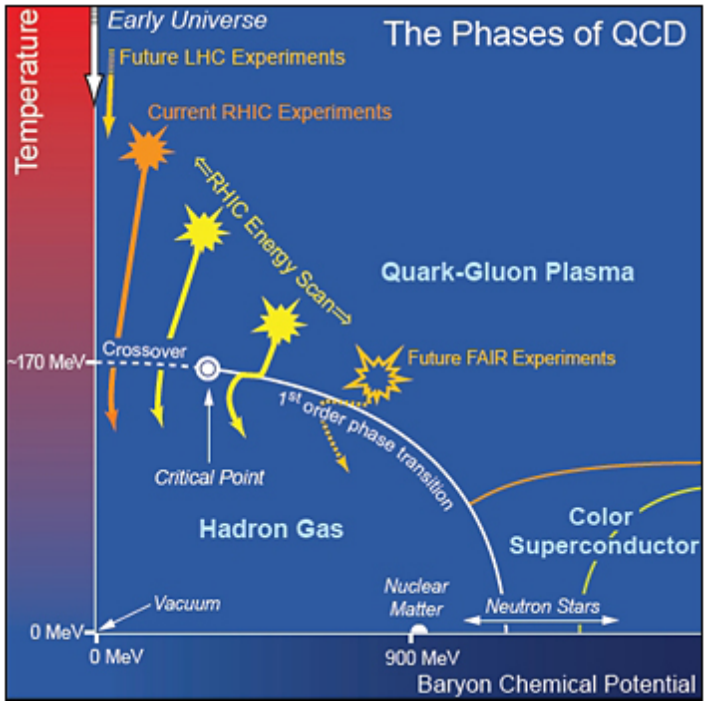

Figure 2.5: Schematic QCD phase diagram for nuclear matter. The solid lines show the phase boundaries for the indicated phases. The solid circle depicts the critical point. Taken from [8].

It is believed that in the first moments of the Universe, a few microseconds after the Big Bang, the temperature and preassure of the matter were sufficient high to create a deconfined state of quarks and gluons - QGP. At the present time, such conditions are not very usual in the nature. One of the places where the QGP should exist is the center of the neutron stars. However, more convenient is to observe the QGP in the early moments of the ultra relativistic heavy-ion collisions. This deconfined medium exists only for a few microseconds so it is nearly impossible to directly observe QGP within this small lifetime. However the detection of various particles in QGP might prove to be useful as signatures and plasma diagnostic tools. It is recognized that there may be no unique signal which will alone lead to the identification of quark gluon plasma. Instead, a number of different signals come out from the medium which may be treated as QGP signatures. These signals include, for example Photons and Dileptons, Strangeness enhancement, J/ψ suppression, Jet Quenching, Elliptic Flow or Heavy Quarks. Some of them will be discussed in the next chapter.

Chapter 3

Heavy-ion collisions

In order to change the hadronic matter into the phase of deconfined quarks and gluons the temperature of the system must be above T_c and density above ϵ_c. To reach such a temperature and density on the Earth, the ultrarelativistic heavy-ion collissions are used. In laboratories like CERN (Geneva, Switzerland), BNL (New York, USA), GSI (Darmstadt, Germany), and GANIL (Caen, France), nuclei are accelerated at energies that range from MeV to TeV beam energies.

3.1 Geometry of heavy-ion collision

Geometry of the collition in relativistic heavy-ion collisions is characterized by a degree of the overlap of two nuclei. The distance parameter $\mid \vec{b} \mid$ is a parameter which characterizes the overlapping region and is defined as the distance between the center of nuclei, where $\vec{b}$ is perpendicular to the beam direction. A pictorial view of relativistic heavy-ion collisions is presented in (Fig.3.1).

In the region of overlapping, the 'participating' nucleons interact with each other, while in non-overlapping region, the 'spectator' nucleons continue along their trajectories [49]. However it is difficult to measure the impact parameter directly in the experiment. Therefore the *centrality* (c) is defined and measured instead of the impact parameter

$$c = \frac{\int_0^b \frac{d\sigma}{da} da}{\int_0^\infty \frac{d\sigma}{da} da}$$

The most central collisions correspond to $\mid \vec{b} \mid \sim 0\, fm$, or in another words, total overlapping of the nuclei. On the other hand, no overlapping area is for the most peripheral collisions correspond to $\mid \vec{b} \mid \sim 2R\, fm$, where R is radius of the nucleus. All centrality classes are shown in (Fig.3.2). Nuclei are Lorenz contracted in beam direction therefore the maximum time of overlapping is determined as $\tau = \frac{2R}{\gamma c}$, where γ is Lorentz factor and c is speed of light.

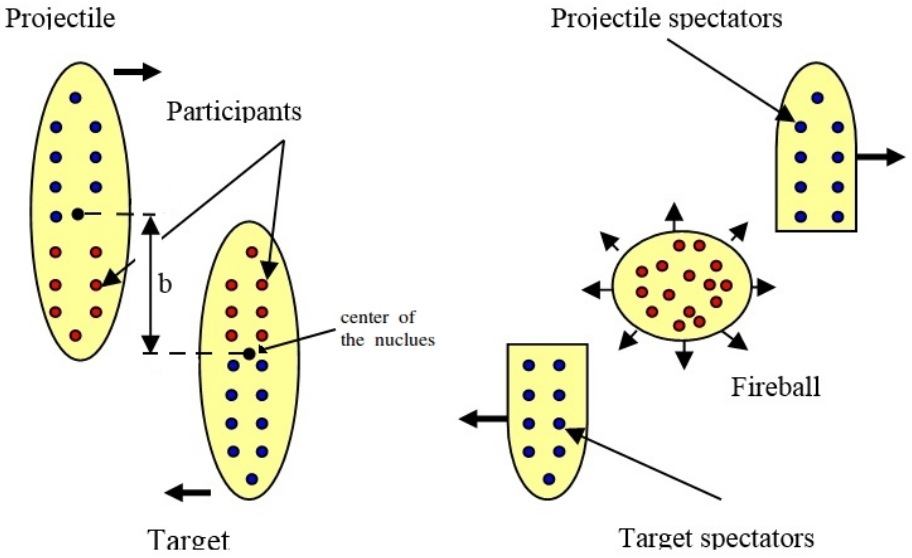

Figure 3.1: Nucleus-nucleus collision with impact parameter b.

3.2 Space-time evolution of the collision

Different phases of evolution of the matter are predicted according to theoretical models and on the basis of data collected so far. Nuclei that are accelerated to ultrarelativistic energies become Lorentz-contracted. In heavy-ion collisions, a large number of nucleons is involved in the processes while the collision takes place in a very tight region.

As is mentioned in previous chapter, the formation of QGP is possible only if critical temperature and energy density are reached. If the system does not reach such conditions after collision of the nuclei then the system will run into a hydrodynamical evolution that is not too interesting in study of QGP, the left side of the (Fig.3.3).

In the right side of the (Fig.3.3), it is shown the evolution of the heavy-ion collision in the case of QGP formation. This evolution can be divided into the following phases.[5]

- Pre-equilibrium - ($t \lesssim 1\, fm/c$), nucleons pass through each other and partons (quarks and gluons) scatters among each other and give rise to an abundant production of deconfined quarks and gluons. During the scattering, partons lose part of their initial energy in the interaction region which is called *fire-ball*. At this stage a large quantity of photons is also produced, *direct photons*, real or virtual. Virtual photons decay in lepton-antilepton pairs.

- Thermalization - ($t \sim 1 - 10\, fm/c$), elastic and inelastic interactions between partons in QGP lead to the thermalization phase. Inhelastic interactions can modify the flavour composition of particles. Due to its internal pressure, the system at thermal equilibrium rapidly expands. While expanding, the system begins to convert into hadron gas. This is the mixed phase of QGP and hadron gas.

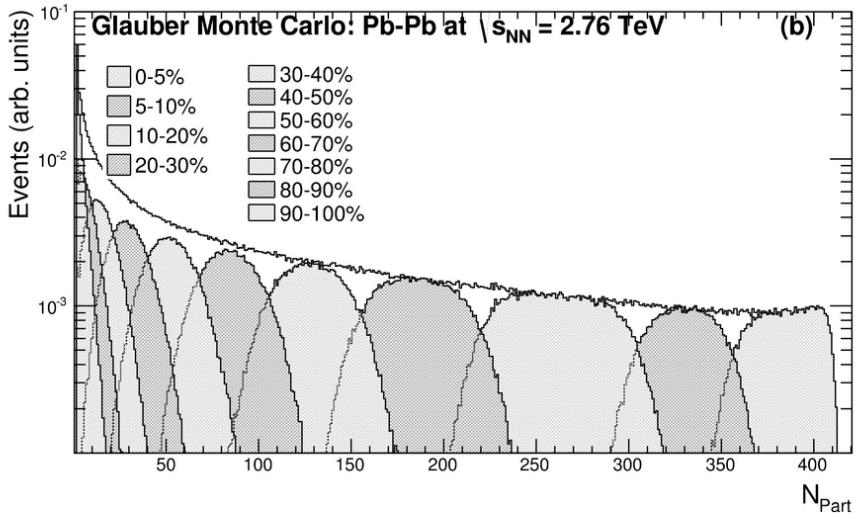

Figure 3.2: Distributions of the number of participants for the corresponding centrality classes from Glauber Monte Carlo calculation. Taken from [23]

- Hadronization - ($t \sim 20\, fm/c$), the expanding system of QGP cools down and reaches the transition temperature. At this point the hadronization begins and quarks and gluons of the QGP condensate into new hadrons.
- Thermal freeze-out - elastic scatterings between hadrons cease and kinematical spectra of the resulting matter also become fixed, After this moment, hadrons fly out freely.

There are three characteristic times during the evolution. The first one is *Initial formation time* (τ_0), at this time the pre-equilibrium stage of the collision ends. The second time is *Chemical freez-out time* (τ_{ch}), where inelastic collisions cease and chemical composition of the matter is fixed. The last one is *thermal freez-out time* (τ_f), when system is so diluted that even elastic collisions cease.

As mentioned above, the only way how we can get any information about the QGP is to inferred them from the properties of the particles remaining after the thermal freez-out. Later, in this chapter, we described some signatures of the QGP.

3.3 Signatures of the QGP

In experiments, after thermal freeze-out, we can obtain information about the early stage of the collision by detection of hadrons. There are observables that can provide information about the early stages of the collisions and possible QGP phase. Some of these observables we will discuss in this section.

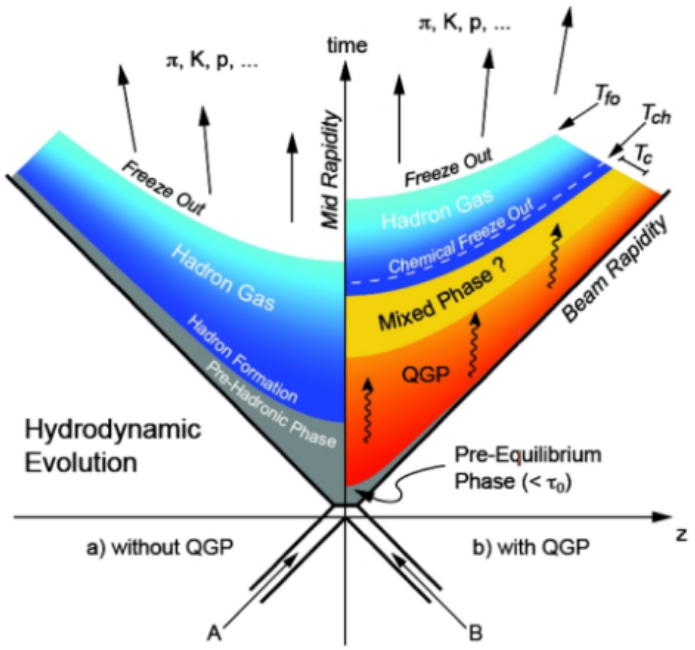

Figure 3.3: Evolution of a central heavy ion collision in a Minkowski-like plane. Taken from [5]

3.3.1 Direct photon

As every thermal source the QGP also emit thermal radiation, real and virtual photons which are produced in quark-antiquark annihilation ($q\bar{q} \rightarrow g\gamma$) and Compton scattering ($g\bar{q} \rightarrow \gamma q$) processes, see in (Fig.3.4). These direct photons and leptons only interact through electromagnetic interaction and have a large mean free path compared to the size of the fireball so they escape the system without re-scattering carrying information on the earliest deconfined stage. [36]

However, to measure direct photons experimentally is difficult because there is also large backgroud of photons which are emitted during the hadronic gas phase. Thanks to this difficulty there is no clear spectra of photons coming from the QGP phase that confirm existence of this phase.

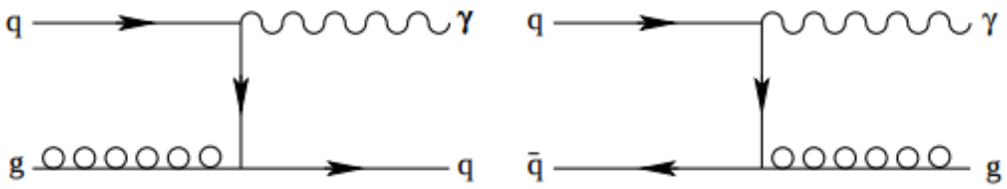

Figure 3.4: Lowest order contributions to photon production from the QGP: Compton scattering (left) and quark-antiquark annihilation (right). Taken from [43]

3.3.2 Strangeness Enhancement

The nuclei, that are used in ultrarelativistic heavy-ion collisions, are made of u and d quarks. Therefore, any strange quarks or antiquarks observed in experiments have been made from the energy of the colliding nuclei. The temperature for dissolving of hadrons is equivalent to the mass of strange quarks and antiquarks. This means that with the high energy and gluons density in the QGP the abundance of strange quarks and antiquarks, produced by gluon fussion, should be enhanced as compared with lower energy and purely hadronic collisions [36]. Therefore, it is important to observe yield and ratios of the strange hadrons at different energies.

The following figure (Fig.3.5) shows the enhancement of strange particles in heavy ion collisions (PbPb collisions at 158 A GeV/c) as compared to pBe collisions at 40 A GeV/c. The enhancement increases with the strange quark content (Ω^-_{sss}, Ξ^-_{dss}, Λ_{uds}) [21].

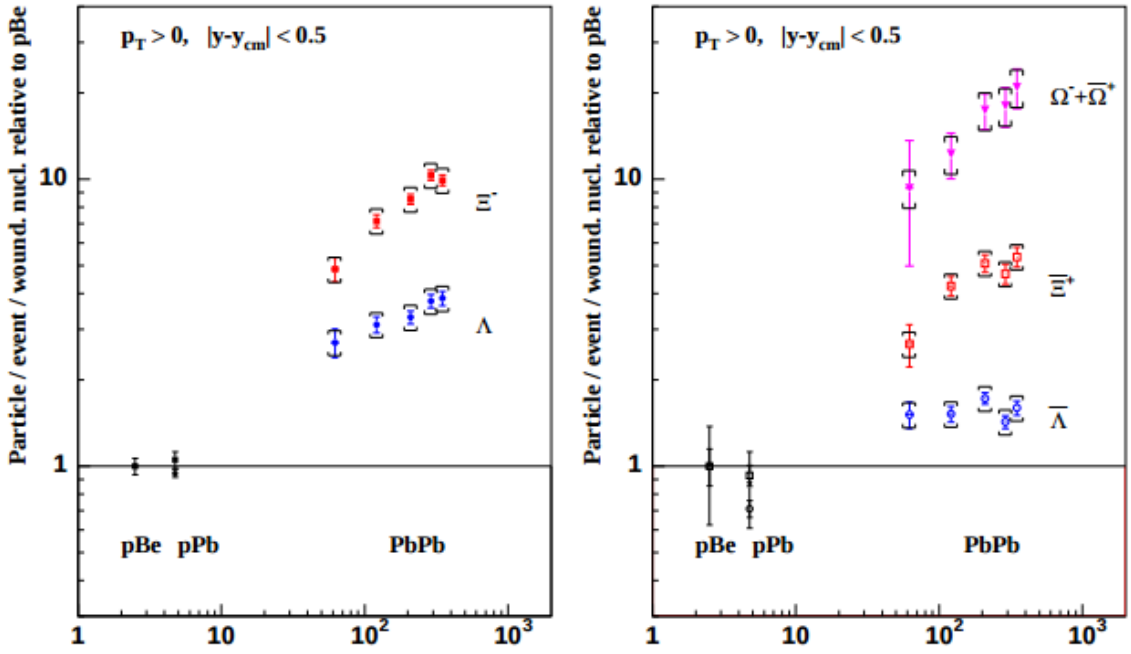

Figure 3.5: Hyperon enhancements E as a function of the number of wounded nucleons at 158 (top) and at 40 (bottom) A GeV/c. Taken from [21]

3.3.3 Flow

Flow is a collective effect of a bulk matter which obviously cannot be produced as a result of superposition of independent nucleon-nucleon collisions [49]. According to class of the collision centrality we can distinguish bewtween isotropic and non-isotropic expansion.

Radial flow

In the case of central collisions there is a symmetry of the initial state in azimuth and overlaping region of the nuclei is circular in the transverse direction ($b \sim 0$). Under such conditions, any pressure gradient causes azimuthally symmetric collective flow of the outgoing particles, which is called 'radial flow' [49]. It is known that the effect of the radial flow in the spectra is well described by the phenomenological hydrodynamical model called blast-wave model in low m_T region [26].

Elliptic flow

In the non-central collisions ($b \nsim 0$) the overlaping region of two nuclei has a spatial anisotrophy like an almond shape as ilustrated in (Fig.3.6, left). Thanks to this spatial anizotrophy the pressure gradient is not azimuthally symmetric and establishes a correlation between momentum and position points [49]. The pressure gradient is bigger in the direction of the short X-axis than in the direction of the long Y-axis. Therefore more particles are emitted to the direction of the short axis. In other words, the spatial anisotropy makes an anisotropy in momentum space as shown in (Fig.3.6, right).

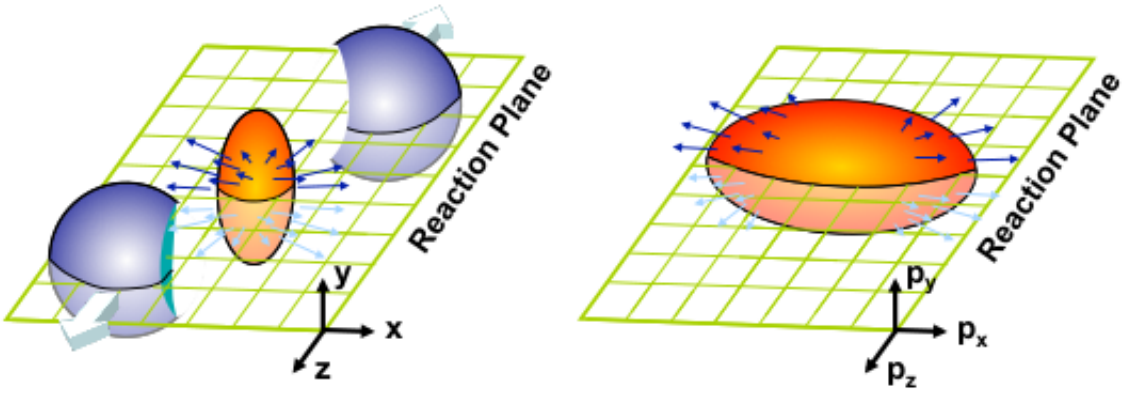

Figure 3.6: **Left** Overlaping region of two nuclei in non-central collisions in coordinate space. **Right** Anizotrophy in momentum space due to spatial anizothophy.

Azimuthal distribution of emitted particles is represented in the form of Fourier expansion

$$\frac{Ed^3N}{dp^3} = \frac{d^3N}{2\pi p_T dp_T dy}[1 + 2v_1 cos(\phi - \Phi_R) + 2v_2 cos[2(\phi - \Phi_R)] + ...]$$

where p_T is the transverse momentum, y is the rapidity, ϕ the azimuthal angle of the outgoing particle, Φ_R is the azimuthal angle of the reaction plane in the laboratory frame. The Fourier coefficient v_1 and v_2 represent the strength of the radia and elliptic flow. The terms ,$sin[n(\phi - \Phi_R)]$, are not included in the Fourier expansion because they

vanish due to the reflection symmetry with respect to the reaction plane, see (Fig.3.7). The reaction plane angle Ψ_R,(Fig.3.7, right), is not known, and is estimated using the transverse distribution of particles in the final state. The estimated reaction plane is called the event plane [30].

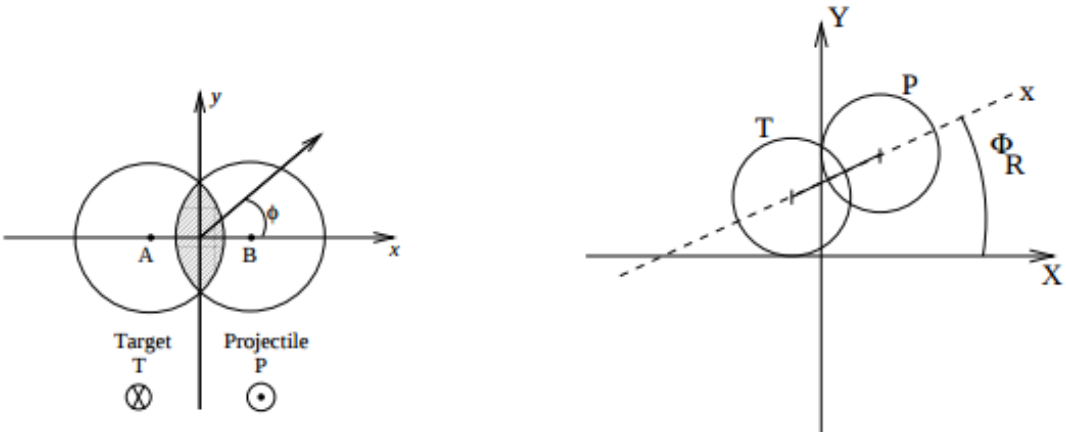

Figure 3.7: **Left** Geometry of the collision and ϕ, the azimuthal angle of one of the outgoing particles. **Right** Φ, the reaction plane angle. Taken from [30]

In the (Fig.3.8) is shown v_2 for charger hadrons as a function of p_T in Au+Au collisions. Solid lines represent a hydrodynamical calculation including a first-order phase transition with a freez-out temperature of $120\,MeV$. In the low p_T region the mass ordering can be seen, that is v_2 for a particle with a lighter mass is larger. This low p_T region is well reproduced by the hydrodynamical calculation. However for higher values of p_T, v_2 saturates and for π,K is smaller than for proton [25].

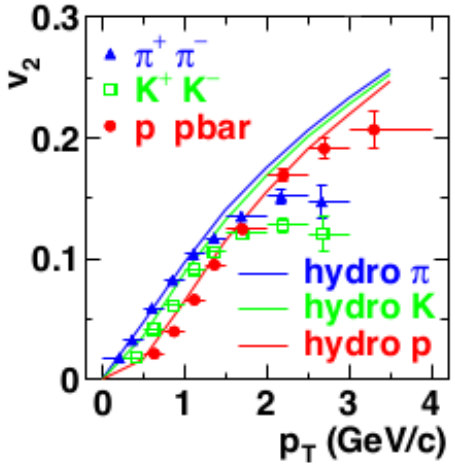

Figure 3.8: v_2 for charged hadrons, π, K, p as a function of p_T in Minimum bias events in Au+Au collisions at s_NN = 200 GeV. Taken from [25]

Chapter 4

STAR experiemnt

The Solenoid Tracker At the RHIC (STAR) is a detector designed to investigate the behavior of strongly interacting matter at high energy density and to search for signatures of quarkgluon plasma (QGP) formation. This experiment is based on the accelerator RHIC in BNL.

4.1 Relativistic Heavy Ion Collider

In present, RHIC is the second-highest-energy heavy-ion collider and the only spin-polarized proton collider which is located at Brookhaven National Laboratory (BNL) in Upton, New York, the United States of America.

It consists of two, hexagonally shaped and $3834\,m$ long circular independent rings in which can be accelerated various ions such as protons or gold nuclei in opposite direction, and collide them at several crossing points around the rings. In this rings, stored particles are deflected and focused by superconducting magnets. There are six interaction points where the two rings cross, allowing the particles to collide. Simple schematic drawing of the RHIC is shown in (Fig.4.1).

The types of particle combinations explored at RHIC to this day are $p+p$, $p+Al$, $p+Au$, $d+Au$, $h+Au$, $Cu+Cu$, $Cu+Au$, $Au+Au$, and $U+U$. The speed of the projectiles is typically 99.995% of the speed of light. For $Au+Au$ collisions, the range of center of mass energy is $7.7-200\,GeV$ per nucleon-pair. The designed luminosity is $2\times10^{26}\,cm^{-2}s^{-1}$ for gold ions and $1.4\times10^{31}\,cm^{-2}s^{-1}$ for protons, however current luminosity for gold ions is $87\times10^{26}\,cm^{-2}s^{-1}$ thanks to stochastic cooling.

Before particles reach te RHIC storage rings they have to pass through several stages of boosters. For protons whole process start in linear accelerator (LINAC), where protons obtain energy of $200\,MeV$. Subsequently, they are sent through the Booster into the Alternating Gradient Synchroton (AGS) where their obtain more energy. When they have sufficient amount of energy, they are injected into the RHIC

storage ring over the AGS-to-RHIC transfer line (AtR). For ions the scenario is little bit different. The heavy-nuclei are first of all partially stripped of their electrons and then injected into Booster by the Electron Beam Ion Source (EBIS). In Booster, particles are more accelerated and stripped of another electrons, then they are injected into the AGS. Here in AGS, ions are stripped of all electrons and also accelerated to sufficient energy in order to be injected into the RHIC storage rings through AtR.

In present, only the STAR detector is running but in the past, there were also PHENIX, BRAMS, PHOBOS detectors but they completed their programmes in 2015, 2006 and 2005 respectively.

Figure 4.1: A schematic drawing of the RHIC accelerator complex. Taken from [11]

4.2 STAR detector

The STAR detector is a flexible detection system that can simultaneously measure many experimental observables. Measurements of the momentum of particles are made at midrapidity over a pseudo-rapidity range $(-1 < \eta < 1)$ with full azimuthal coverage $(0 < \Phi < 2\pi)$. Identification of particles is also made in range $(-1 < \eta < 1)$. The detector system contains the TPC, SVT, EMC, TOF, external TPC, solenoid magnet, electronics, data acquisition, and trigger as major systems. The detection system consists of TPC and SVT inside a soleniodal magnet to enable tracking, momentum analysis, particle identification via dE/dx and location of primary and secondary vertices. STAR magnet has an outer radius of 3.66 m and a length of 6.85 m and is capable to produce a uniform magnetic field of $0.25 - 0.5$ T along the beam axis [4].

There are also forward detectors, such as the Beam-Beam Counter (BBC) and the Endcap Electromagnetic Calorimeter (EEMC). Around the STAR magnet is located the Moun Telescope Detector (MTD) which covers 45 % of azimuthal angle in range

$(-0.5 < \eta < 0.5)$. The MTD, the primary Vertex Position Detector (pVDP) and the Zero Degree Calorimeter (ZDC) are located outside of the magnetic field.

In 2014, Heavy Flavor Tracker (HFT) detector was installed. It is the innermost detector of the system which consists of three detectors. The outermost part of HFT is a doubled-sided silicon strip detector (SSD), the intermediate silicon tracker (ITS) is a silicon pad detector and the innermost detector is the pixel detector (PXL) which is composed of MAPS technology [3].

In following figure (Fig.4.2) the sketch of the STAR detector can be seen.

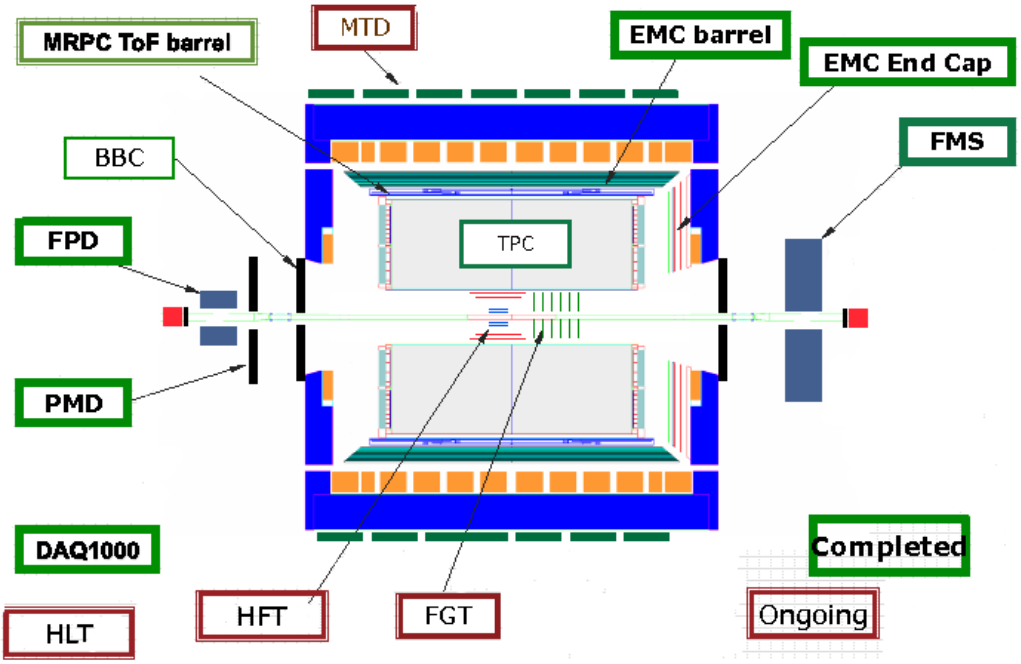

Figure 4.2: The sketch of the STAR detector system. Taken from [3]

For our work the most important detectors of the STAR detector are TPC and ToF. For event selection the trigger system is used which is based on the pVPD and ZDC. Following subsections will describe these parts.

4.2.1 TPC detector

TPC is a part of the STAR detector which records the tracks of particles, measures their momenta and identifies the particles by measuring their ionization energy loss. Its pseudo-rapidity range covers $(-1.8 < \eta < 1.8)$ with full azimuthal coverage $(0 < \Phi <$

2π) and over the full range of multiplicities. Particles are identified over a momentum range from $100\,MeV/c$ to greater than $1\,GeV/c$ and momenta are measured over a range of $100\,MeV/c$ to $30\,GeV/c$.

The TPC is situated in a large solenoidal magnet that operates at $0.5\,T$. It surrounds the beam-beam interaction region and its drift volume is limited by 2 concentric field cage cylinders, of radii $50\,cm$ and $200\,cm$ with the length $4.2\,m$. The STAR TPC is shown schematically in (Fig.4.3). The paths of primary ionizing particles passing through the gas volume are reconstructed with high precision from the released secondary electrons which drift to the readout end caps at the ends of the chamber. The uniform electric field which is required to drift the electrons is defined by a thin conductive Central Membrane (CM) at the center of the TPC, concentric field-cage cylinders and the readout end caps.

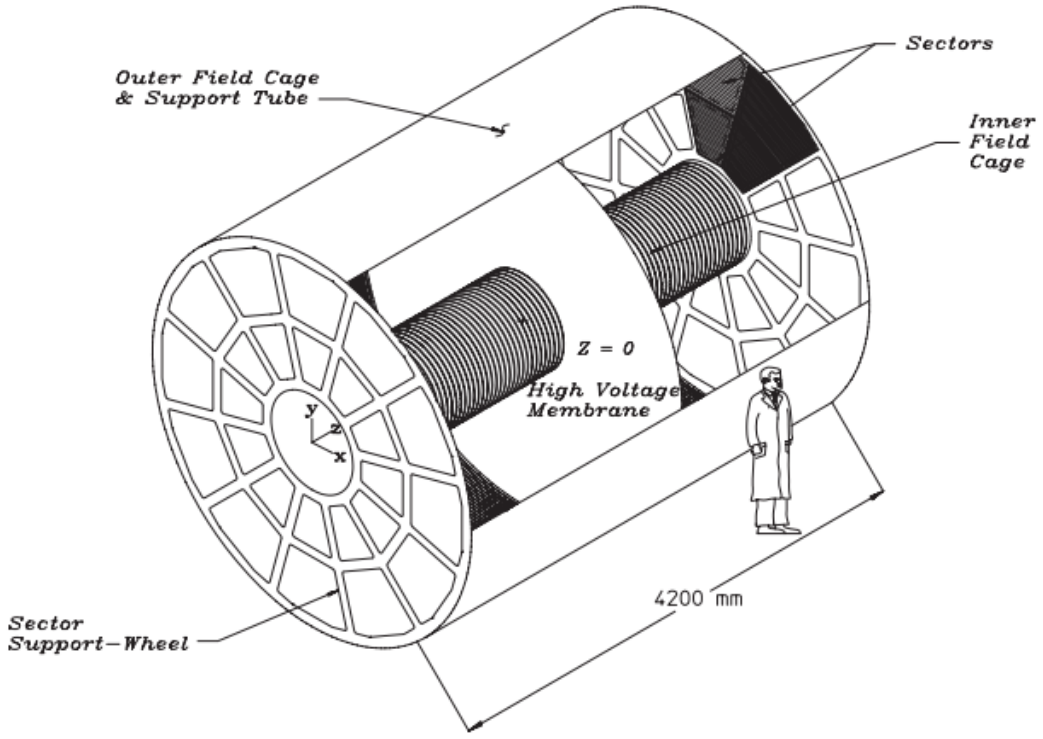

Figure 4.3: STAR TPC overview. Taken from [37]

The TPC is filled with P10 gas (10% methane, 90% argon) regulated at 2 mbar above atmospheric pressure and the gas circulates with rate of $36,000\,l/h$ (full volume of the TPC is $50,000\,l$). The main property of this gas is a fast drift velocity which peaks at a low electric field. There is a central membrane held at $28\,kV$ that, together with the equipotential rings along the inner and outer field cage, create a uniform drift field of $135\,V/cm$ from the central membrane to the ground end caps where the readout chambers are located.

The readout system is based on Multi-Wire Proportional Chambers (MWPC) and

consists of 12 sectors. Each sector is divided into the inner and outer subsector with 13 and 32 pad rows, respectively. While the outer subsection has continuous pad coverage for better dE/dx resolution and contains in total of 3942 pads with dimensions $6.2 \times 19.5\,mm$, the inner subsection is designed for precise tracking and consists of 1750 pads with size of $2.85 \times 11.50\,mm$. The inner subsection has small pads arranged in widely spaced rows, since each pad in row 1 through 8 and in row 8 through 13, respectively is separated by the $48\,mm$ and $52\,mm$ space. The detailed schema can be found in (Fig.4.4).

By passing of charged particles through the volume of the P10 gas, the atoms of the gas are ionized. The ionization electron drifts towards the endcaps at a constant velocity of $\sim 5.45 cm/\mu s$ and hence maximum drift time in the TPC is $\sim 40 \mu s$. The drifting electrons avalanche in the high fields at the $20\,\mu m$ anode wires providing an amplification of 1000 to 3000. The induced charges from the avalanche are then collected by the several read-on pads.

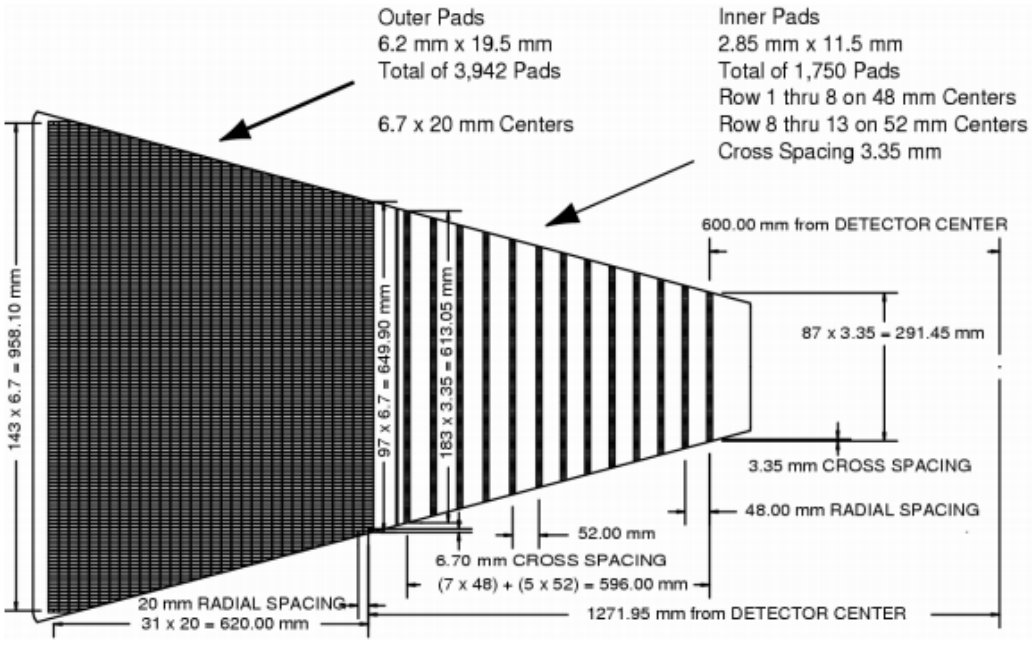

Figure 4.4: The anode pad plane with one full sector shown. The inner sub-sector is on the right and it has small pads arranged in widely spaced rows. The outer sub-sector is on the left and it is densely packed with larger pads. Taken from [37]

Performance of the TPC

The track of an infinite-momentum particle passing through the TPC at mid-rapidity is sampled by 45 pad rows, but a finite momentum track may not cross all 45 rows. It depends on the radius of curvature of the track, the track pseudorapidity, fiducial

cuts near sector boundaries, and other details about the particle's trajectory. While the wire chambers are sensitive to almost 100% of the secondary electrons arriving at the end-cap, the overall tracking efficiency is lower $(80-90\%)$ due to the fiducial cuts, track merging, and to lesser extent bad pads and dead channels. There are at most a few percent dead channels in any one run cycle [37].

The track of a primary particle passing through the TPC is reconstructed by finding ionization clusters along the track. The clusters are found separately in x, y and in z space. The local x axis is along the direction of the pad-row, the local y axis extends from beam-line outward through the middle of an perpendicular to the pad-rows, the local z axis lies along the beam axis. These clusters are split using an algorithm then looks for peaks with a valley between them and then ionization is divided between the two tracks.

Particle identification by TPC

Energy loss in the TPC gas is a valuable tool for identifying particle species. It works especially well for low momentum particles but as the particle energy rises, the energy loss becomes less mass-dependent and it is hard to separate particles with velocities $v > 0.7c$. STAR is able to separate pions, kaons and protons with a very good accuracy up to $1.2\,GeV/c$. This requires a relative dE/dx resolution of 7% [37].

Energy loss of charged particles by ionization, mentioned above, can be calculated using the Bethe-Bloch formula

$$-\left\langle \frac{dE}{dx} \right\rangle = 2\pi N_A r^2 mc^2 \rho \frac{Z}{A}\frac{z^2}{\beta^2}[ln(\frac{2mc^2\beta^2 W_{Max}}{I^2}) - \beta^2 - \frac{\delta^2}{2}] \tag{4.1}$$

where N_A is Avogadro's number, r is classical radius, m is mass of particle, c is speed of light in vacuum, ρ is density of the material, Z and A are atomic number and weight of material, W_{Max} is maximum energy transfer in a single collision, I is mean excitation energy and δ is density correction.

(Fig.4.5) shows the energy loss for particles in the TPC as a function of the particle momentum. As can be seen, the energy loss for particles is mass ordered which means that heavier particles lose more energy in comparison to the lighter for the same momentum.

4.2.2 ToF

In the STAR experiment, the particle identification is done by TPC thanks to its wide and azimuthally complete acceptance about the collision zone. However, it has a problem to identify the charged hadrons such as π & K, (p) if their momentum is above $\sim 0.7\,(1.0)\,GeV/c$. Therefore, the Time Of Flight (TOF) system, with a total timing

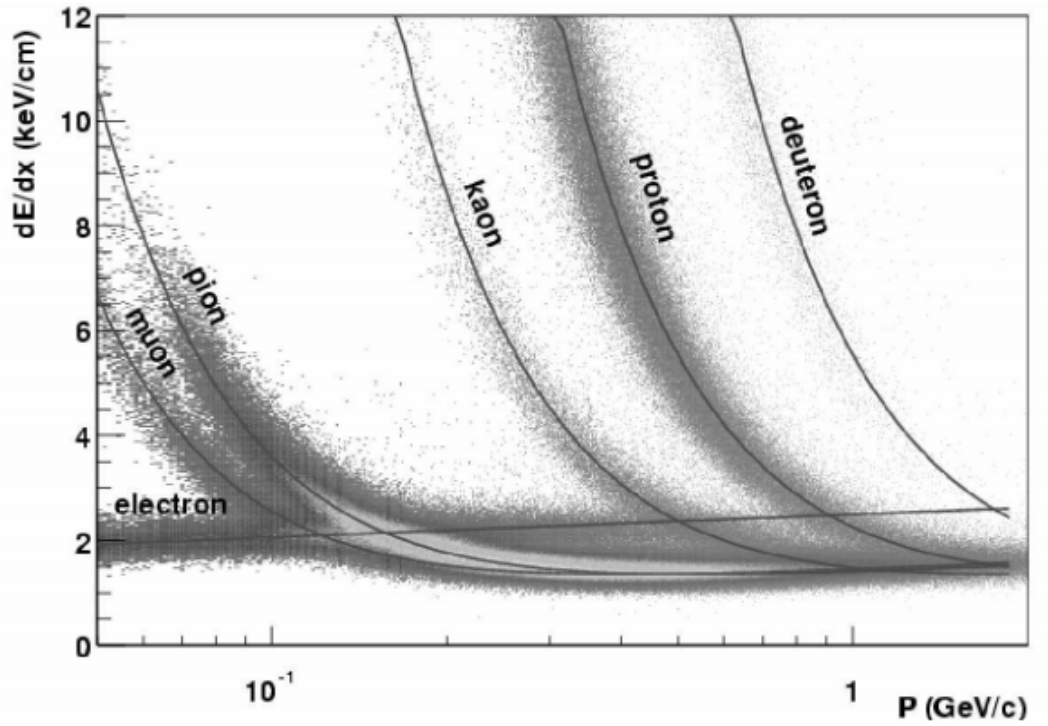

Figure 4.5: The energy loss distribution for primary and seconday particles in the STAR TPC as a function of the p_T of the primary particle. The magnetic field was $0.25\,T$. Taken from [37]

resolution of $100\,ps$ in the STAR geometry, was developed to improve the particle identification ability of the STAR experiment for the particles with momenta in range $0.6 - 3\,GeV/c$. The system was fully installed in 2010.

The system consists of two separate detector subsystems, one called the Pseudo Vertex Position Detector (pVPD) and the other called the Time of Flight Patch (TOFp). Detector (pVPD) is the start detector and the Time-Of-Flight Patch (TOFp) is the stop detector. The electronic signals from these detectors define the time intervals of interest for particle Time of Flight measurements. The pVPD consists of two identical detector assemblies that are positioned very close to the beam pipe and outside the STAR magnet. The TOFp sits inside the STAR magnet immediately outside the TPC, see in (Fig.4.6). The signals from these detectors are carried to electronics racks on the so-called South Platform next to STAR for digitization and interfacing with the STAR data stream. For more details see [35].

Particle identification by ToF

Digitization is done versus a clock, and those digitized signals are subtracted, as

$$(stop\ \ time - clock) - (start\ \ time - clock) = stop\ \ time - start\ \ time \equiv \tau \qquad (4.2)$$

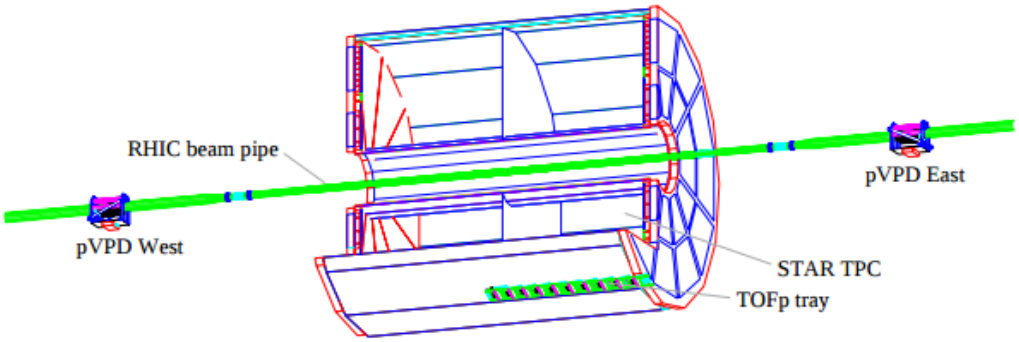

Figure 4.6: A scale drawing of the locations of pVPD and TOFp detectors in relation to the STAR TPC and the RHIC beam pipe. Taken from [35]

so long as the clocks used on both the start and stop sides are the same to $10 - 20\,ps$ in every event. The Leading edge time is sampled by $25\,ps$ binning [44].

This time τ, is associated with reconstructed tracks in the STAR TPC by track extrapolation to the TOF detectors. The TPC detector provides the momentum p, and total length L, so we can calculate inverse velocity [12]

$$\frac{1}{\beta} = \frac{c\tau}{L} \tag{4.3}$$

where c is speed of light. From the relativistic particle momentum we obtain

$$p = m\beta\gamma \Rightarrow p^2 = \beta^2(m^2 + p^2) \tag{4.4}$$

where m is particle mass, one can derive the relation between β and p where the only one unknown parameter is the mass of the particle

$$\frac{1}{\beta} = \sqrt{(\frac{m^2}{p^2} + 1)} \tag{4.5}$$

(Fig.4.7) shows behavior of $1/\beta$ as a function of momentum. Solid black lines are predictions from (4.5) for π, K and p.

4.2.3 Trigger system

It is a pipelined system which is based on the input from the fast detectors to control the event selection for slower tracker detectors. This system is divided into four different layer levels - from 0 to 3. Interactions that pass selection criteria in these four successive trigger levels are sent to storage [20].

Level 0 is the fastest and analyzes raw data to determine whether a requested type of interaction occured in crossing. To decribe the interaction one requires to detect particle multiplicity and distribution of the particles in η, σ space. Data that are in this

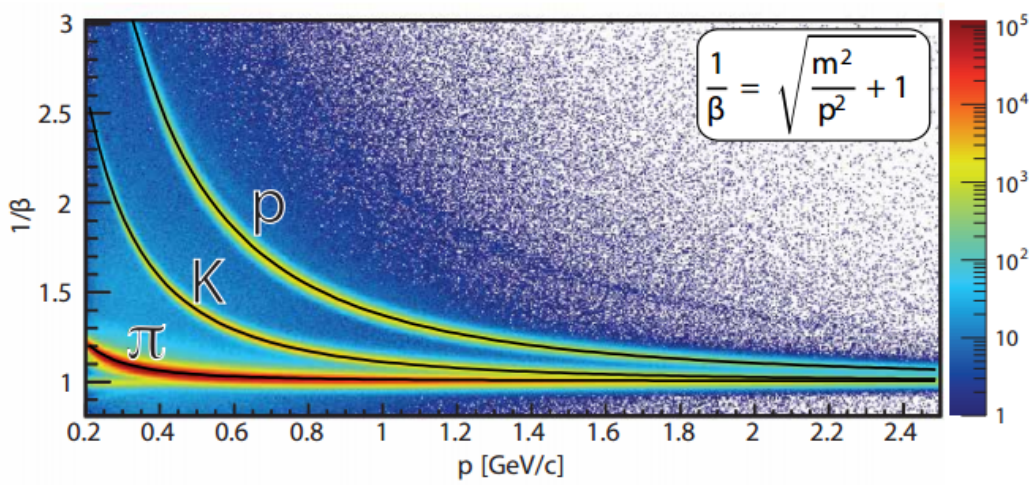

Figure 4.7: Particle Identification by STAR TOF. Taken from [44]

level are mostly from the Zero Degree Calorimeter (ZDC), Beam Beam Counter(BBC), Multi-Wire Counter (MWC) and The Central Trigger Barrel (CTB). When the data pass through Level 0 they reach another levels. Level 1 and 2 operate in the time period of several milliseconds during which these data are more detailed analyzed in order to determine whether the event meets more finely grained criteria. If it does not, then the digitization process is aborted and the detectors are free for a new trigger. The last, Level 3 makes the final decission. If the data pass through this level so they will be sent to storage.

ZDC decetors are located at nearly identical positions along the beamlines on the both side of the intersection regions at the distance of $18.25\,m$ outside of the RHIC magnet. Due to this magnet the charged particles are deflected from zero degree region which means that they are not measured by ZDCs. Therefore, ZDCs measure the energy of the neutral particles mainly non-interacting spectator neutrons but also from collisions. There are three modules in the ZDC detector where each module consists of a series of tungsten plates alternating with layers of wavelength shifting fibers that route Cherenkov light to a photo-multiplier (PMT). The CTB is the detector consists of 240 scintilator slats which cover the outer shell of the TPC. Its pseudo-rapidity range covers $(-1 < \eta < 1)$. These slats are divided into 4 cylindrical bands where each band cover $1/2$ unit of psudo-rapidity. It triggers on the flux of charged particles in the midrapidity region [20]. BBC detector is a set of scintillator installed around the RHIC beam pipe. It consists of two parts which are situated on the EAST and WEST pole of the STAR magnet, $3.75\,m$ from the center of interaction region, see in (Fig.4.2). It is a versatile tool for polarized proton beam diagnostics. The BBC setup provides an excellent minimum bias trigger and it covers pseudo-rapidity range $3.4 <\mid \eta \mid < 5.0$ .For more technical details about BBC, see [46].

Chapter 5

Femtoscopy

In this chapter we will look on the basics of quantum interference of two identical particles which is also known as Hambury-Brown and Twiss (HBT) interferometry. We will describe historical and theoretical background of the femtoscopy and then application in particle physics.

5.1 Brief history of femtoscopy

In 1956 Robert Hambury-Brown and Richard Q. Twiss introduced a novel method based on photon intensity interferometry, which was an alternative way to Michelson interferometry how to measure sizes of the stellar objects.

In their experiment two photo-detectors are placed in the far field zone of a chaotic radiation source. A correlation between the signals from the two detectors is measured. Hambury and Twiss found that photons emitted by thermal source are not independent. Such a far field zone with photo-detectors is shown in (Fig.5.1). Inner part of the

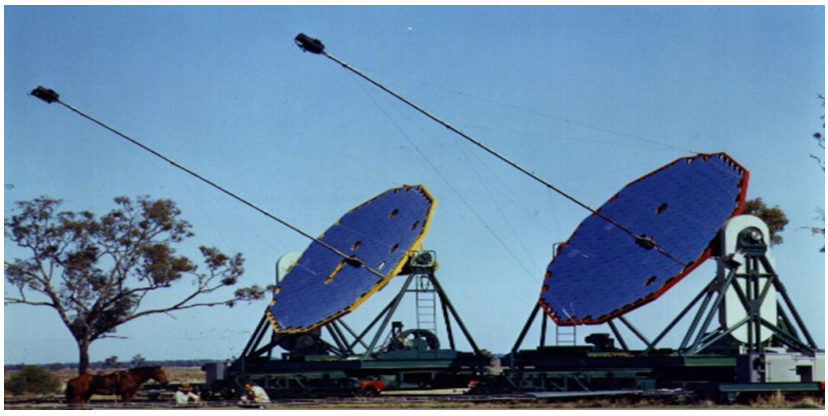

Figure 5.1: The Hambury Brown-Twiss intensity interferometer at Narrabri, New South Wales, Australia. Taken from [9]

detectors were covered by mirrors with diameter of 156 cm. These mirrors focused

light from the star into the cathode of the photomultipliers. The output signals from both photomultipliers were processed and afterwards the correlation function between the intensity of the photons, which were received by the mirrors, could be obtained.

In particle physics, somewhat similar technique was used by Gerson Goldhaber, Sulamith Goldhaber, Wonyong Lee and Abraham Pais in the 1960s. In proton and anti-proton collisions they observed an angular correlation between identical pions and using the symmetrized wave funtion for identical pions they reproduced the angular distribution. They concluded that this effect originated from the quantum statistical effect which is called Bose-Einstein correlation [38]. In 1970s G. I. Kopylov and M.I.Podgoretsky developed the theoretical background and mathematical formalism of two particle correlation. Because of typical space and time extents of order of tens fermi the term **"Femtoscopy"** has been used.

5.2 Intensity interferometry of two identical particles

Here we will describe theoretical overview of intensity interferometry of two identical particles and its application in heavy ion collisions.

Suppose that we have a certain source which emits two identical particles from different points, x_1 and x_2. This source is characterized by the emission function $S(x,p)$ which can be viewed as the probability that particle with four-momentum p is emitted from the space-time point x in the collision region, so if we want to know probability that source emits one particle with momentum p we have to integrate over the whole source

$$P(\vec{p}) = \int dx^4 S(x,p)|_{p_0=E_p}, \tag{5.1}$$

where emission funtion is evaluated on-shell i.e. $p_0 = E_p = \sqrt{m^2+\vec{p}^2}$. We also assume that there is no final state interaction between particles. These emitted particles are observed by two detectors that are located at x'_1 and x'_2. In (Fig.5.2) we can see that there are two possible routes, shown as solid and dashed lines, how paticles can reach detectors. In a case of identical particles there is no way how to distinguish between them in quantum mechanics, therefore we have to symmetrize the wave funtion for the case of bosons or antisymmetrize for the case of fermions.

$$\begin{aligned} \Psi_{12}(x_1,x_2) &= \frac{1}{\sqrt{2}}[\Psi_1(x_1)\Psi_2(x_2) \pm \Psi_1(x_2)\Psi_2(x_1)], \\ &= \frac{1}{\sqrt{2}}[A_1A_2e^{-ip_1(x_1{}'-x_1)}e^{-ip_2(x_2{}'-x_2)} \pm A_1A_2e^{-ip_1(x_1{}'-x_2)}e^{-ip_2(x_2{}'-x_1)}], \end{aligned} \tag{5.2}$$

where $\Psi_i(x_i)$ is a wave funtion for a single particle emitted from point x_i with a momentum p_i and A_i is an amplitude. The signs $(\pm)$ correspond to symmetrized or

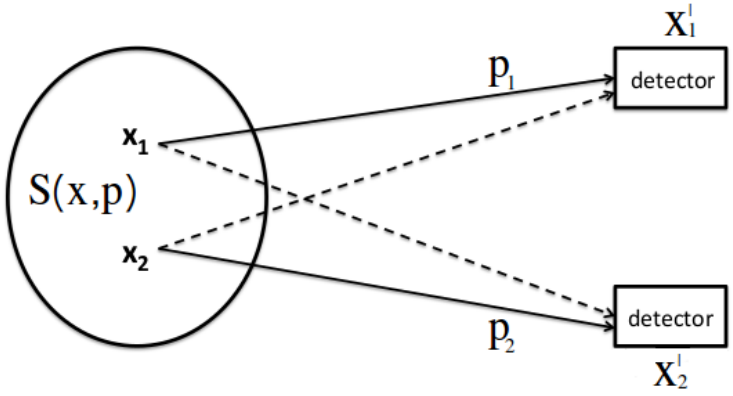

Figure 5.2: Diagram of quantum interference between two identical particles.

anti-symmetrized funtion. The positive sign is for symmetrized funtion (bosons) while the negative sign is for anti-symmetrized funtion (fermions).

Then the probability density is written as

$$\mid \Psi_{12}(x_1, x_2) \mid^2 = \frac{1}{2} \mid A_1 \mid^2 \mid A_2 \mid^2 [2 \pm e^{i(x_1-x_2)(p_1-p_2)} \pm e^{-i(x_1-x_2)(p_1-p_2)}], \tag{5.3}$$

$$= \mid A_1 \mid^2 \mid A_2 \mid^2 [1 \pm cos((p_1 - p_2)(x_1 - x_2))], \tag{5.4}$$

where the second term in (Eg. 5.4) represents the strength of the correlation in HBT effect. Therefore the correlation becomes strong when the relative difference r or relative momentum q are small and on the other hand, there is almost no correlation for large values of q and r.

Now, it is appropriate to define the correlation function C_F as

$$C_F(\vec{p_1}, \vec{p_2}) = \frac{P(\vec{p_1}, \vec{p_2})}{P(\vec{p_1})P(\vec{p_2})}, \tag{5.5}$$

where $P(\vec{p_1}, \vec{p_2})$ is the probability of measuring two particles with momenta p_1 and p_2 and $P(\vec{p_i})$ is the probability of measuring of a single particle with momentum p_i. Probability $P(\vec{p_1}, \vec{p_2})$ is described as

$$P(\vec{p_1}, \vec{p_2}) = \int d^4x_1 d^4x_2 S(x_1, p_1) S(x_2, p_2) \mid \Psi_{12} \mid^2 . \tag{5.6}$$

Using (Eq. 5.4) in (Eq. 5.6) we obtain

$$P(\vec{p_1}, \vec{p_2}) = P(\vec{p_1})P(\vec{p_2}) \pm \int d^4x_1 d^4x_2 S(x_1, p_1) S(x_2, p_2) cos((p_1 - p_2)(x_1 - x_2)). \tag{5.7}$$

In this point, it is good to define relative and average four-momentum and space-time coordinate as follow

$$q = (p_1 - p_2) \qquad k = \frac{1}{2}(p_1 + p_2), \tag{5.8}$$

$$x = (x_1 - x_2) \qquad X = \frac{1}{2}(x_1 + x_2). \tag{5.9}$$

If we assume that the emission function has a smooth momentum dependence we can write

$$S(x_1, p_1)S(x_2, p_2) = S(X + \frac{x}{2}, k + \frac{q}{2})S(X - \frac{x}{2}, k - \frac{q}{2}) \approx S(X + \frac{x}{2}, k)S(X - \frac{x}{2}, k) \tag{5.10}$$

This step is the so-called **smoothness approximation** and it is only valid for sufficiently small relative momenta.

Using the mentioned smoothness approximation, relative and average variables we can rewrite (Eq. 5.7) as follow

$$P(\vec{p_1}, \vec{p_2}) = P(\vec{p_1})P(\vec{p_2}) \pm \int d^4x \; cos(xq) \int d^4X \; S(X + \frac{x}{2}, k)S(X - \frac{x}{2}, k), \tag{5.11}$$

where the term $\int d^4X \; S(X + \frac{x}{2}, k)S(X - \frac{x}{2}, k) = D(x, k)$ is called the **relative distance distribution** which gives us information about the source.

Then, the two-particle correlation function (Eq. 5.5) can be written as

$$C_F(\vec{q}, \vec{k}) = 1 \pm \frac{\int cos(xq)D(x, k)d^4x}{\int d^4x d^4X S(X + \frac{x}{2}, k)S(X - \frac{x}{2}, k)} = 1 \pm \frac{\int cos(xq)D(x, k)d^4x}{\int D(x, k)d^4x} \tag{5.12}$$

where term $\frac{D(x,k)d^4x}{\int D(x,k)d^4x} = d(x, k)$ is a normalized relative distance distribution. Using term $d(x, k)$ in (Eq. 5.12) we obtain

$$C_F(\vec{q}, \vec{k}) = 1 \pm \int cos(xq)d(x, k)d^4x \tag{5.13}$$

From the equation (Eq.5.13) can be seen that there is a one to one relation between the emission and correlation function, in which the correlation function is 4-dimensional fourier transform of the emission function. However, to get information about emission function from correlation function is quite difficult issue, because of measured particles are on-shell, $p^0_{1,2} = E_{1,2} = \sqrt{(m^2 + p^2)}$, while the four-momenta q and k are off-shell and satisfy the relation

$$k \cdot q = \frac{1}{2}(m_1^2 - m_2^2). \tag{5.14}$$

Here, we introduce **on-shell approximation** which is used in many application

$$k^0 \approx E_k = \sqrt{m^2 + k^2}. \tag{5.15}$$

Using the on-shell approximation and asking for the (Eq. 5.14) to be equal to zero we get that only three of four relative momentum components are kinematically independent. Hence, the q-dependence of $C(\vec{q}, \vec{k})$ allows to test only three of four independent x-directions of the emission function [47].

This requirement is so-called **mass-shell constraint** and using it we obtain a condition for the fourth variable of the four-momentum q in the form

$$q^0 = \frac{\vec{k}}{k^0} \cdot \vec{q} = \vec{\beta} \cdot \vec{q}. \tag{5.16}$$

With the mass-shell constraint, (Eq.5.13) can be written as

$$C(\vec{q}, \vec{k}) = 1 \pm \int cos(\vec{q} \cdot \vec{x})\, d\vec{x} \int d(\vec{x} + \vec{\beta}t, t, k)\, dt = 1 \pm \int cos(\vec{q} \cdot \vec{x}) S_{\vec{k}}(\vec{x}), \tag{5.17}$$

where function $S_{\vec{k}}(\vec{x})$ is defined as the **relative source funtion**. In a case when the system is in the rest frame of the particle pair where $\beta = 0$, the relative source function is a simple integral over the time argument of the relative distance distribution $d(\vec{x}, t, k)$ [47]. Here the correlation function is fourier transformation of the relative source function into which the time dependence is convoluted. The deconvolution of the time (t) and space ($\vec{x}$) variables must be done through models that describes four-dimensional particle emission.

It is very useful to parametrize the source by a function for which its fourier transformation has an analytic form. Here we assume that the spatial distribution is the Gaussian distribution

$$S(x, p) = \frac{1}{\sqrt{2\pi R^2}} exp(-\frac{x^2}{2R^2}) \tag{5.18}$$

where R is the standart deviation (source radius). Since the fourier transform of Gaussian distribution is also Gaussian distribution, the correlation function can be expressed analytically as follow

$$C(\vec{q}, \vec{k}) = 1 \pm exp(-q^2 R^2(\vec{k})). \tag{5.19}$$

Thus the correlation function is written as function of the relative momentum q and the standard deviation R of a gaussian distribution of the particles-emitting source. This obtained standart deviation R is usually called the **HBT radius**.

For one-dimensional analysis we use correlation function which is written as s function of a Lorentz-invariant relative momentum q_{inv}

$$C(\vec{q}, \vec{k}) = 1 \pm exp(-q_{inv}^2 R_{inv}^2(\vec{k})), \tag{5.20}$$

where R_{inv} is a one-dimensional source size and q_{inv} is defined as

$$q_{inv}^2 = q_x^2 + q_y^2 + q_z^2 - q_0^2, \tag{5.21}$$

$$q_0 = E_1 - E_2, \tag{5.22}$$

where q_i is the relative momentum in each direction of the coordinate space and q_0 is the energy difference between two particles, where the energy is dedined as $E = \sqrt{m^2 + p^2}$. This one-dimensional analysis is usually performed in case of limited statistics and all spacial and temporal information are convoluted into $R_{inv}(\vec{k})$.

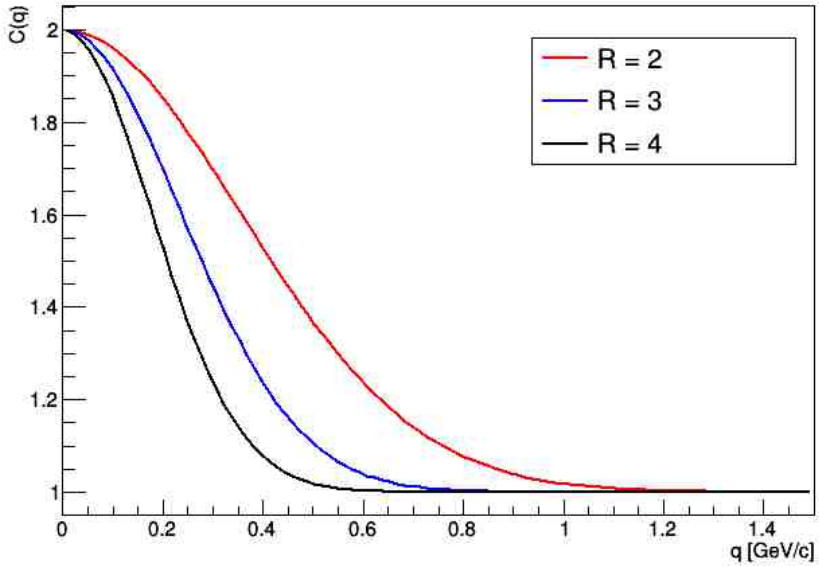

Figure 5.3: Correlation function constructed according to (Eq. 5.19) for three different values of the source radius.

5.2.1 Bertsch-Pratt parametrization

For extraction of spatial information about the particle emitting source, the standard Cartesian coordinate system is not the best. The most common coordinate system for femtoscopic measurements is the so-called Bertsch-Pratt coordinate system often known as the **out-side-long system**. In this system, the relative momentum is decomposed into sideward (q_{side}), outward (q_{out}) and longitudinal (q_{long}) direction.

The longitudinal direction is parallel to the beam direction which is typically in z-direction, outward direction is parallel to the pair transverse momentum $k_T = (p_{T1} + p_{T2})/2$ and sideward direction is perpendicular to both longitudinal and outward directions. Such a decomposition can be seen in (Fig.5.4). The Bertsch-Pratt coordinate system is hence unique for each pair of particles.

Each vector $\vec{V}$ can be decomposed into the Bertsch-Pratt coordinate system as follow

$$\begin{aligned} V_{long} &= V_z \\ V_{out} &= \frac{(P_x V_x + P_y V_y)}{P_T} \\ V_{out} &= \frac{(P_x V_x - P_y V_y)}{P_T} \end{aligned} \tag{5.23}$$

where $P = (P_0, P_x, P_y, P_z)$ is pair momentum and $P_T^2 = (P_x^2 + P_y^2)$.

The correlation femptoscopy of identical particles is usually constructed in the Longitudinal Center of Mass System (LCMS) of the emitted pair where $p_{z1} + p_{z2} = 0$, the

component of pair momentum in long direction vanishes, therefore q_0 can be rewritten as follow

$$q_0 = E_1 - E_2 = \frac{\vec{p_1} + \vec{p_2}}{E_1 + E_2} \cdot (\vec{p_1} - \vec{p_2}) = \vec{\beta} \cdot \vec{q} \overset{\text{LCMS}}{\approx} \beta_T q_{out} \tag{5.24}$$

where $\vec{\beta} = (\beta_T, 0, \beta_l)$ and $q = (q_{out}, q_{side}, q_{long})$. In LCMS the term $\beta_l = 0$. Thus the LCMS frame can be obtained by the boost from the laboratory frame along the longitudinal axis. Additional boost of the LCMS frame in the out direction provides the Pair Rest Frame (PRF). The correlation of non-identical parcticles are studied in the PRF. In the PRF, both particles have the same momentum $\vec{k}^* = \vec{k}_1 = -\vec{k}_2$ and hence the relative pair momentum is $q = 2\vec{k}^*$.

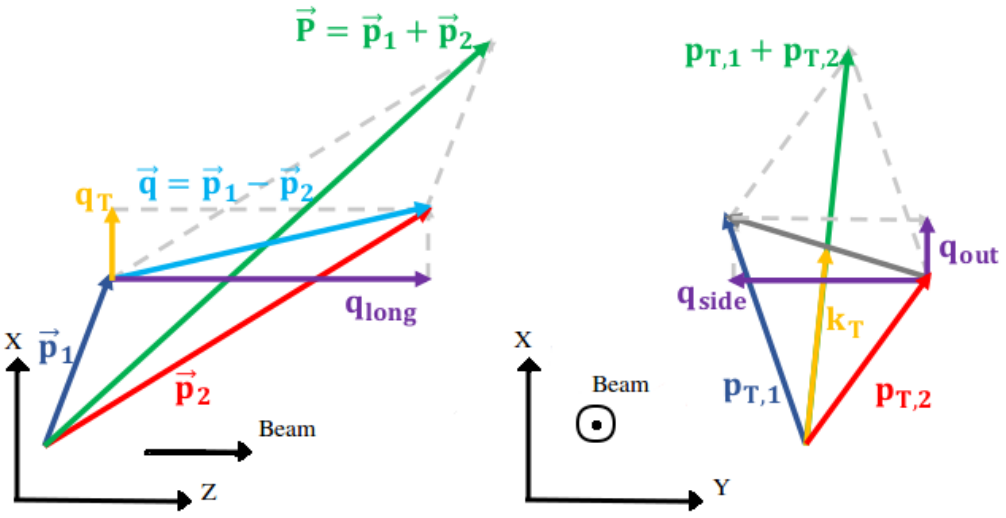

Figure 5.4: The decomposition of $\vec{q}$ in Pratt-Bertsch coordinates.

In the Bertsch-Pratt parametrization, the most general form of correlation function of two identical particles for a Gaussian source is expressed as

$$C(\vec{q}, \vec{k}) = 1 \pm exp(-q^\mu q^\nu R^2_{\mu\nu}), \tag{5.25}$$

where μ and ν take *out*, *side* and *long*. $R^2_{\mu\nu}$ denotes the six HBT radii parameters which have general form as follow

$$\begin{aligned}
R^2_{out} &= \langle(\tilde{x} - \beta_T \tilde{t})^2\rangle \\
R^2_{side} &= \langle\tilde{y}^2\rangle \\
R^2_{long} &= \langle(\tilde{z} - \beta_l \tilde{t})^2\rangle \\
R^2_{out,side} &= \langle(\tilde{x} - \beta_T)\tilde{y}\rangle \\
R^2_{out,long} &= \langle(\tilde{x} - \beta_T \tilde{t})(\tilde{z} - \beta_l \tilde{t})\rangle \\
R^2_{side,long} &= \langle(\tilde{z} - \beta_l)\tilde{y}\rangle
\end{aligned} \tag{5.26}$$

where $\tilde{x} = \Delta x = (x - \langle x \rangle)$, β_l, β_T are the components of the pair velocity and $\langle ... \rangle$ denotes an average with the emission function

$$\langle f \rangle(k) = \frac{\int d^4x \, f(x) S(x,k)}{\int d^4x \, S(x,k)} \tag{5.27}$$

For an azimuthally integrated analysis, the emission function has a reflection symmetry $\tilde{y} \to -\tilde{y}$. This symmetry translates to a $q_s \to -q_s$ symmetry of the two-particle correlation function. This means that the cross-terms $R^2_{out,side} = R^2_{side,long} = 0$. If we choose as the reference frame the LCMS frame of the pair, where $\tilde{z} \to -\tilde{z}$, then $R^2_{out,long} = 0$. Afterwards, the correlation function is in the form of

$$C(\vec{q}, \vec{k}) = 1 \pm \lambda(\vec{k}) exp(-q^2_{out} R^2_{out}(\vec{k}) - q^2_{side} R^2_{side}(\vec{k}) - q^2_{long} R^2_{long}(\vec{k})), \tag{5.28}$$

where HBT radii measure the spatial and temporal extend of the collision system at the freeze-out.

Here, we also define another parameter, the overal strength of the correlation, $\lambda(\vec{k})$. The name of this parameter from history is **chaoticity parameter**, it generally accounts for particles identification, long-lived decays or long-range tails in the separation distribution. The value of chaoticity parameter is between 0-1. This $\lambda(\vec{k})$ parameter is unity for a fully chaotic source and smaller than unity for a source with partially coherent particles emission.

It is appropriate to mention that the azimuthally sensitive analysis can be also performed, we will discuss it later in this thesis.

5.2.2 Final State Interaction

During the derivation of correlation function in the previous subsection we assumed that there is only Bose-Einstein or Fermi-Dirac interference effect and no final state interaction between the emitted particles. However, most HBT measurements in heavy ion collisions are performed with charged particles therefore these particles feel long range Coulomb interaction effects on the way from the source to the detector. Moreoever, particles also feel the total electric charge of the source from which they are emitted. Another kind of interaction which plays an important role between outgoing particles is the strong interaction. This interaction is very important in proton-proton correlation. Therefore, if we want to have more correct description of the correlation function, the interaction must be taken into account.

In our analysis only the Coulomb interaction between outgoing particles plays an important role. Interaction between particles and the source is negligible and strong interaction is also sufficiently small so it can be also ignored.

Coulomb interaction

AS mentioned above, in the case of charged particles the Coulomb interaction between particles can not be neglected. This interaction causes a suppression for like-sign particles while for unlike-sign it causes an enhancement of the measured correlation function at low $\vec{q}$.

To calculate the strength of the Coulomb interaction, we consider Schrödinger equation [36] which contains the Coulomb potential

$$[\frac{\hbar^2\nabla^2}{2\mu} + \frac{Z_1 Z_2 e^2}{r}]\Psi_c(\vec{q},\vec{r}) = E\Psi_c(\vec{q},\vec{r}), \tag{5.29}$$

where μ is the reduced mass and r is the relative distance between the two particles, Z_1 and Z_2 are protons numbers of particles, e is the elementary charge and E is the energy in the center of mass frame.

The solutions of the (Eq. 5.29) are written in terms of the confluent hypergeometric function F as follow

$$\begin{aligned} \Psi_c(\vec{q},\vec{r}) &= \Gamma(1+i\eta_\pm)e^{-\frac{1}{2}\vec{q}\cdot\vec{r}}F(-i\eta;1,z_\pm), \\ z_\pm &= \frac{1}{2}qr(1\pm cos(\theta)). \end{aligned} \tag{5.30}$$

where θ is the angle between $\vec{q}$ and $\vec{r}$, $\eta_\pm$ is the Sommerfield parameter which depends on the particle mass and charge as

$$\eta_\pm = \pm\frac{me^2}{4\pi q}, \tag{5.31}$$

where minus (plus) sign is for unlike-sign (like-sign) particles. Then the symmetrized Coulomb wave function is

$$\Psi_r(\vec{q},\vec{r})\frac{1}{\sqrt{2}}(\Psi_c(\vec{q},\vec{r}) + \Psi_c(\vec{q},-\vec{r})). \tag{5.32}$$

When we put this wave function to the (Eq. 5.6), then the contribution from the Coulomb interaction to the correlation function can be calculated as follow

$$P_c(\vec{q},\vec{r}) = \frac{1}{2}\int d\vec{r}\rho(\vec{r}) \mid \Psi_r(\vec{q},\vec{r}) \mid^2, \tag{5.33}$$

where $\rho(\vec{r})$ is the distribution of the average distance between the particles in each pair as they are emitted [36].

In the (Fig.5.5) we can see an example how interactions typically contribute into the proton-proton correlation function.

5.3 Particle correlation of non-identical particles

Up to now we have considered only emission of identical particles for which the average value of the projection of the separation vector in the PRF on any direction is equal

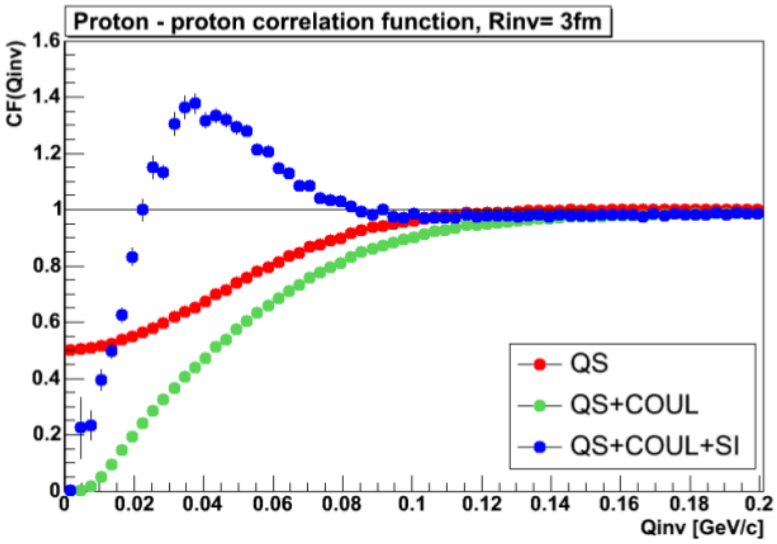

Figure 5.5: Proton-proton correlation functions for the source size of 3 fm with interactions. Taken from [49].

to zero due to symmetry. However, there are also cases when the emitted particles are non-identical. For these situations one can study space-time asymmetries in the emission. These asymmetries will lead to the non-zero average value of the projection of the separation vector.

Before we start, we emphasize that each vector with sign $(*)$ is in the PRF. As in the case of identical particles we assume, that Coulomb interaction dominates. Under these circumstances the correlation function takes the form [32]

$$C(\vec{p}_1, \vec{p}_2) = A_c(\eta)[1 + 2\frac{\langle r^*(1 + cos(\theta^*))\rangle}{a_c}], \tag{5.34}$$

where θ^* is an angle between $\vec{k}^*$ and $\vec{r}^*$ vectors, a_c is Bohr radius which depends on the charges of the particles, A_c is the Coulomb factor and $\langle ...\rangle$ denotes averaging which is defined as 5.27.

For example, let us have opposite-sign particles. The term $(1 + cos(\theta^*))$ is always positive, while Bohr radius a_c is negative. Therefore, the term $2\langle r^*(1 + cos(\theta^*))\rangle/a_c$ will be negative and will decrease the correlation. The decrease depends on the θ^* angle. So, if the vectors $\vec{k}^*$ and $\vec{r}^*$ are aligned, $(cos(\theta^*) > 0)$, then the correlation is weaker and for opposite pointing vectors, $(cos(\theta^*) < 0)$, the correlation is stronger.

The problem is that we can measure only $\vec{k}^*$ vector, the method for measuring $\langle \vec{r}^* \rangle$ vector is not apparent. However, there is another way because we know how to measure the total pair momentum $\vec{P}$. The pairs of correlated particles can be divided into two groups:

1. $\vec{k^*}$ and $\vec{P}$ are aligned $\rightarrow cos(\Psi) > 0$
2. $\vec{k^*}$ and $\vec{P}$ are pointing in opposite direction $\rightarrow cos(\Psi) < 0$

where angle Ψ is between $\vec{P}$ and $\vec{k}^*$. The main idea is sketched in (Fig.5.6). If the consideration is restricted to the transverse plane, the angle ϕ between vectors $\vec{r}^*$ and $\vec{P}$ is connected to the other two by a simple relation

$$\Psi = \phi + \theta^*. \tag{5.35}$$

From these three angles only Ψ angle can be measured experimentally. Here we define

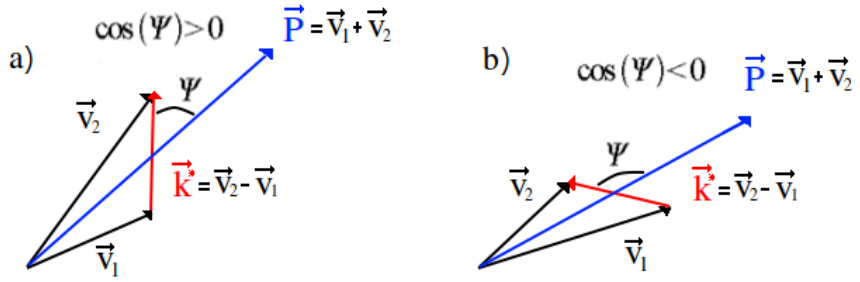

Figure 5.6: Asymmetry in space-time emission seen by non-identical particle correlations.

two functions. The first one is with pairs having $cos(\Psi) > 0$ and we will denote it as C^+. The second function is for pairs with $cos(\Psi) < 0$ which is denoted with C^-. In the most of the analysis, the ratio of these functions is performed C^+/C^- as can be seen in (Fig. 5.7).

One can simply say that in case that the second particle is faster than the first one, $cos(\Psi) > 0$, then the correlation is weaker because the first particle never catches up the second particle. This fact corresponds with the left case in the (Fig.5.6). In the second case, the first particle is faster then the second one, $cos(\Psi) < 0$. This first particles catches up the second particle. For this case the correlation is stronger and this fact corresponds to the right case in the (Fig.5.6). There is also assumption that different particles do not origin from the same point, see below.

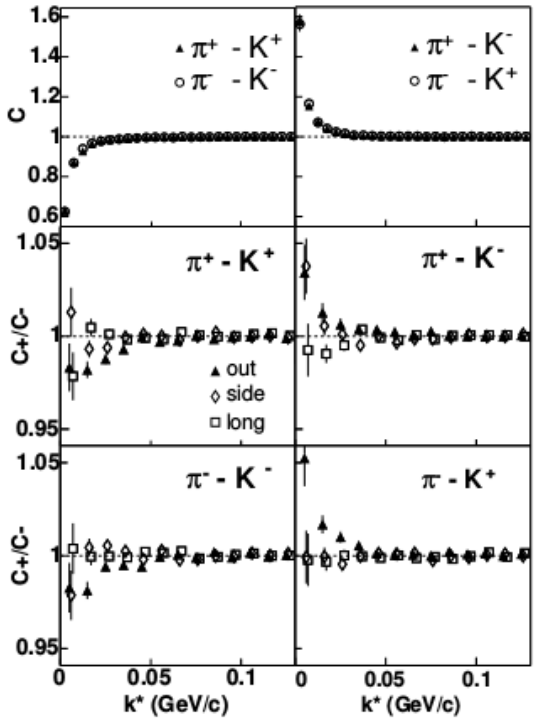

Figure 5.7: Pion-kaon correlation functions which are constructed from central Au+Au STAR data taken at $\sqrt{s_{NN}} = 130\,GeV$ by the STAR detector at RHIC. Top panel: correlation function $C(\vec{k}^*)$ for various pair combination. Middle and botton panel: double ratio of correlation function $C^+(\vec{k}^*)$ and $C^-(\vec{k}^*)$. Taken from [15]

5.4 Femtoscopy and dynamical system

Up until now in our analysis, we have considered a case in which source was static. In this case the size of static source measured by femtoscopy is the same as the whole source size because particles are emitted towards random direction with their thermal momenta from the source thus there is no correlation between the spatial and momentum distributions. However in case of the heavy-ion collisions, femtoscopy does not measure the whole source size but it measures the so-called **homogeneity region**, which is defined as an area that emits particles with small $\vec{q}$, for ilustration see (Fiq.5.8).

The reason that these homogeneity regions do not correspond to the whole size of the source is that in heavy ion-collisions one can watch that lengths of these regions (HBT radii) depend on the quantities such as pair momentum, size of the whole source and reaction plane.

Pair momentum

Here we assume that system is in LCMS frame and that the particles are emitted to radial direction from the center of the source with velocity $\vec{\beta}_T(\vec{r})$. It is also assumed

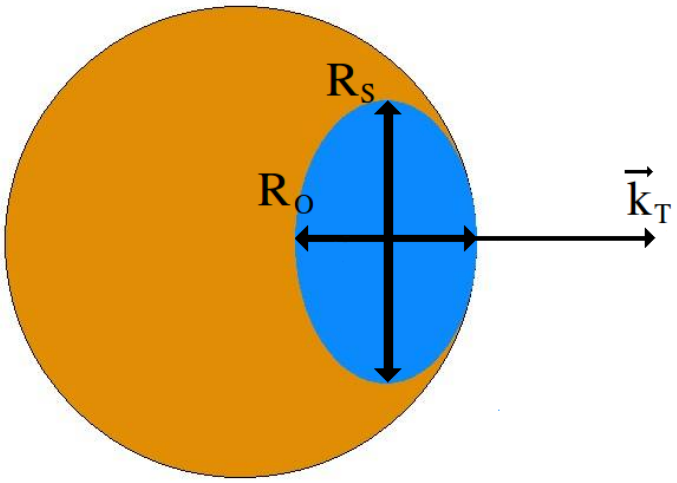

Figure 5.8: Whole source (yellow) with homogeneity region (blue) for pair momentum.

that the transverse velocity of particles is proportional to the distance from the center of the source to their particle positions. Therefore the particles around the surface of the source get larger momentum and thus the emission region measured as the HBT radius would correspond to a smaller region around the surface for higher k_T, and a larger region for lower k_T, see (Fig. 5.9). In the limit of $k_T = 0$ the HBT radii become closer to the whole size of the source [38].

Within a simple model with a Gaussion source approximation based on the hydrodynamics, the HBT radii are explicitly written as a function of k_T (m_T) as follows

$$R_s^2(m_T) = \frac{R_{geom}^2}{1 + m_T \eta_f^2 / T}, \tag{5.36}$$

$$R_o^2(m_T) = R_s^2(m_T) + \frac{1}{2}(\frac{T}{m_T})^2 \beta_T^2 \tau_0^2, \tag{5.37}$$

$$R_l^2(m_T) = \tau_0^2 \frac{T}{m_T} \frac{K_2(m_T/T)}{K_1(m_T/T)}, \tag{5.38}$$

where R_{geom} is the actual source size, η_f is the flow rapidity, T is the temperature, β_T is the trnsverse pair velocity, τ_0 is the freeze-out time and K_n is the n-th modified Bessel function [48]. However the presence of the k_T dependence of the HBT radii indicate the dynamical expansion of the source.

Size of the system

In the case of hadron-hadron correlation, one can show that the extracted HBT radii should depend on the quantity which represents the system size, such as centrality or multiplicity.

In the (Fig. 5.10) the centrality dependence of pion source parameters are shown as a function of $m_T = \sqrt{m_\pi^2 + k_T^2}$ for six different centralities. We can see that for

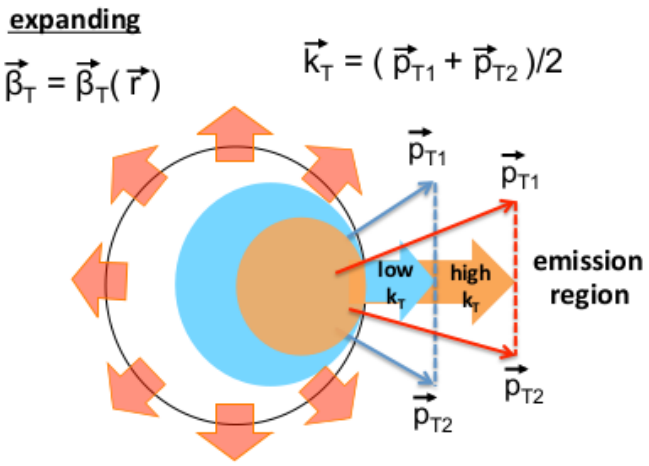

Figure 5.9: Expanding source with two different homogeneity regions. Taken from [38].

more central collisions the HBT radii are bigger which is consistent with initial source size because for more central collisions the overlap of two nuclei is greater. Here we can also see that with increasing of m_T the HBT radii are decreasing that is consistent with pair momentum dependence which was mentioned before.

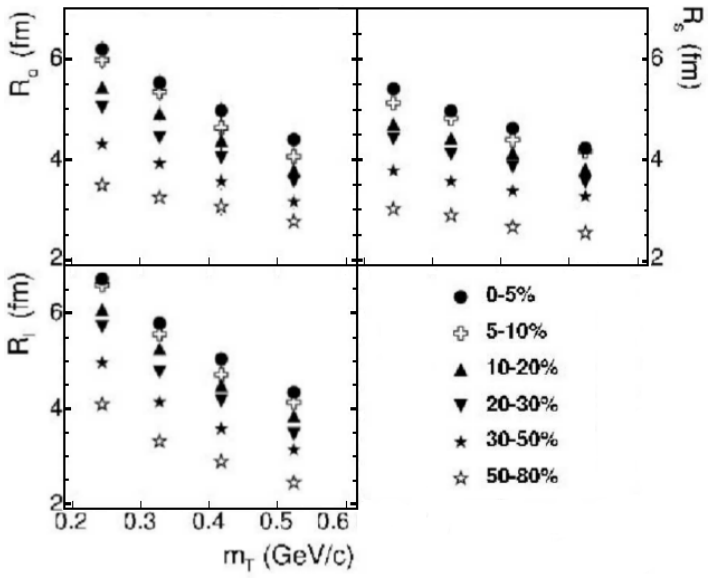

Figure 5.10: HBT parameters vs m_T for different 6 centralities. Data from Au+Au collisions at $\sqrt{s_{NN}} = 200\,Gev$. Taken from [36].

In the (Fig. 5.11) we can see that HBT radii are linearly scaled well with the 1/3 power of the number of participants N^{part} calculated by Glauber model. Here the value N_{part} corresponds to the volume of the source and hence $N_{part}^{1/3}$ corresponds to the radius of the source [38].

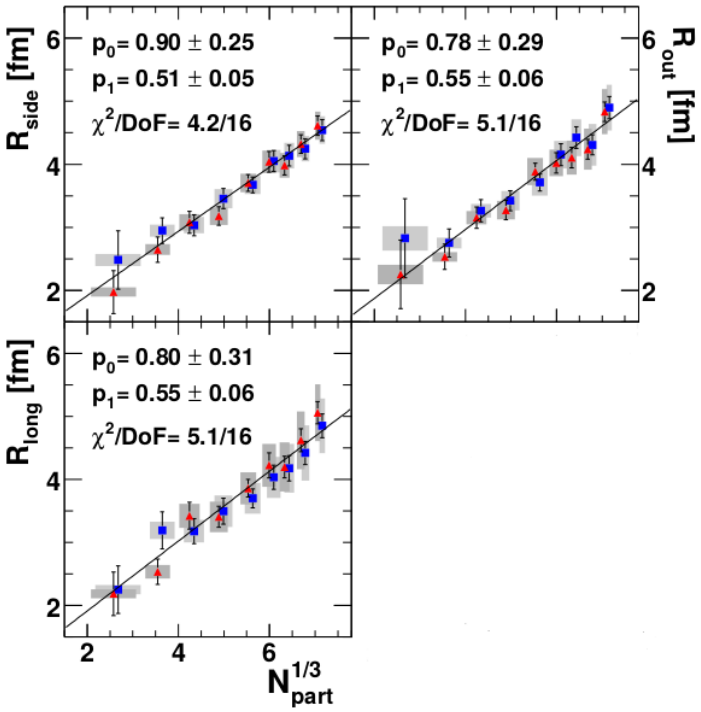

Figure 5.11: The HBT radii for positive (blue square) and negative (red triangle) pion pairs as a function of $N_{part}^{1/3}$ in Au+Au collisions at $\sqrt{s_{NN}} = 200\,GeV$ measured by PHENIX experiment. Taken from [24].

Reaction plane

In the subsection Flow (2.3.3), we wrote down that for non-central collisions the source shape is expected to be an elliptical shape, see in (Fig. 2.6). The initial spatial anisotropy creates the momentum anisotropy in the final state which is called elliptic flow and the expansion of the source is prefered into the in-plane direction. In that case one can measure the shape of the source at freeze-out by studying oscillation of the HBT radii with respect to the reaction plane. In the (Fig. 5.12) we can see that lengths of the HBT radii R_s and R_o are different with respect to the reaction plane. In general, the Φ dependence of the HBT radii is described by

$$R^2_\mu(k_T,\Phi) = R^2_{\mu,0}(k_T) + 2\sum_{n=2,4,6...} R^2_{\mu,n}(k_T)cos(n\Phi) \qquad \mu = o,s,l,ol \qquad (5.39)$$

$$R^2_\mu(k_T,\Phi) = R^2_{\mu,0}(k_T) + 2\sum_{n=2,4,6...} R^2_{\mu,n}(k_T)sin(n\Phi) \qquad \mu = os \qquad (5.40)$$

where $R^2_{\mu,n}$ are the n^{th} orger Fourier coefficients for radius term μ. These coefficient can be computed as follow

$$R^2_{\mu,n}(k_T) = \langle R^2_\mu(k_T,\Phi)cos(n\Phi)\rangle \qquad \mu = o,s,l,ol \qquad (5.41)$$

$$R^2_{\mu,n}(k_T) = \langle R^2_\mu(k_T,\Phi)sin(n\Phi)\rangle \qquad \mu = os \qquad (5.42)$$

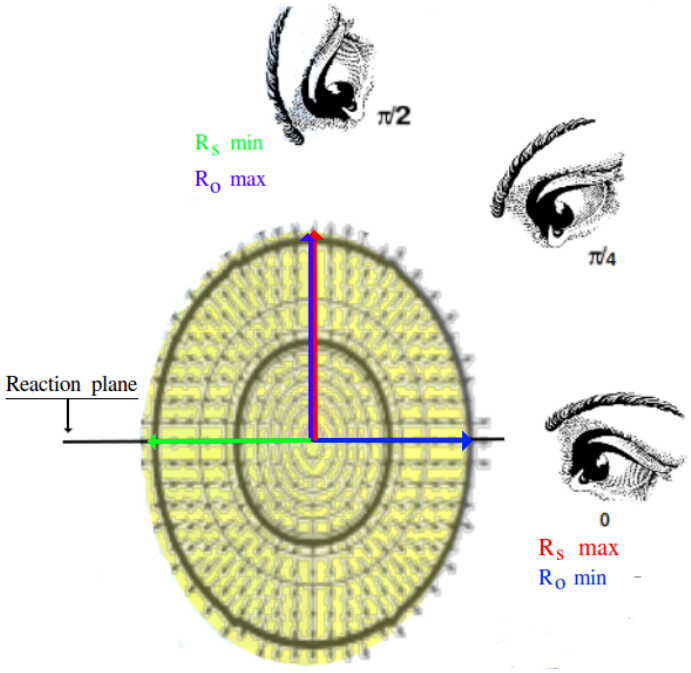

Figure 5.12: A view on the HBT radii from different angle respect to the reaction plane.

The 0^{th} order Fourier coefficients are expected to be nearly identical to radii extracted in an azimuthally integrated analysis. For more detail you can see [18]. In the (Fig. 5.13) we can see measurements of dependence of squared HBT radii on the reaction plane angle with respect to 2^{th} order for three centrality classes from STAR experiment.

HBT puzzle

For describing of transverse momentum distribution and elliptic flow at low $p_T < 2\,GeV/c$ a relativistic hydrodynamics could be used. Therefore it was natural to expect that this hydrodynamics could reproduce the observables of HBT interferometry dominated by two particles with low momentum. In spite of the fact that variety of hydrodynamic models have been calculated, none of them was not able to describe the HBT radii from experiments. In the (Fig. 5.14) we can see some models which are inconsistent with the data from Au+Au collisions at $\sqrt{s_{NN}} = 200\,GeV$ measured at RHIC. A problem is that according to calculations the ratio R_o/R_s, which is sensitive to the emission duration, should be much larger value than unity but the experimental data almost shows unity. It is clear that models significantly overpredict this ratio. Models also either underestimate or overestimate values of R_o, R_l and R_s. This failure of hydrodynamic models in describing the HBT results from heavy ion collisions is called the **HBT Puzzle** that has not been solved for a decade. Recently however,

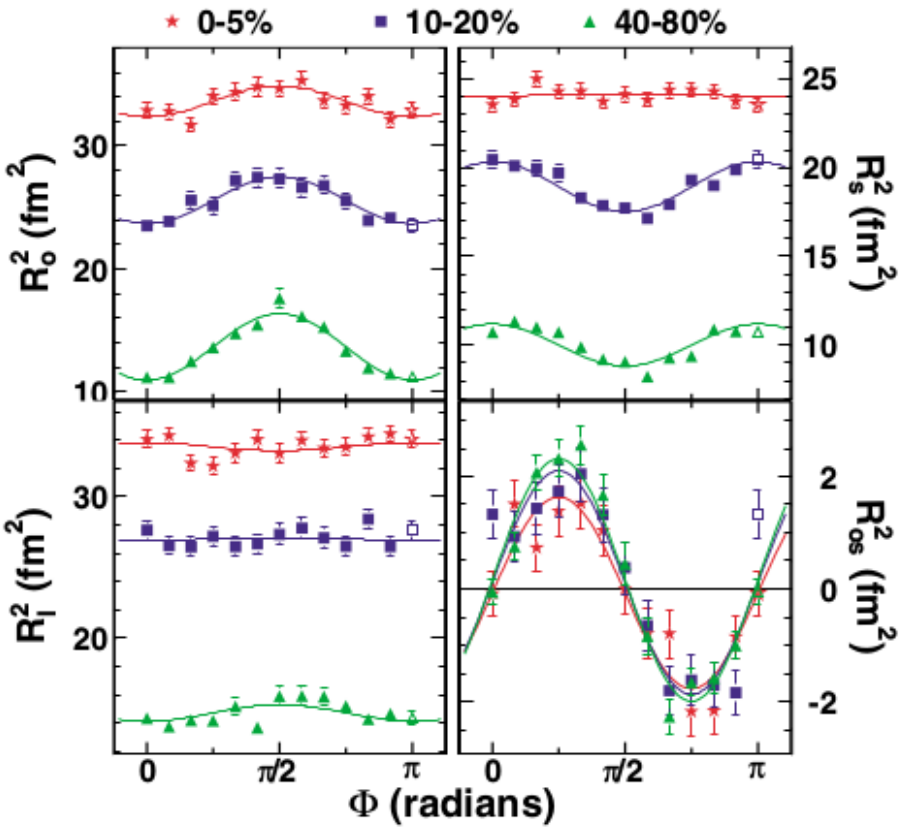

Figure 5.13: Squared HBT radii using radii relative to the reaction plane angle for three different centrality classes from Au+Au collisions at $\sqrt{s_{NN}} = 200\,GeV$. Taken from [16].

Pratt provided a possible explanation of this puzzle, see [40], [41].

Blast-wave model

As we mentioned above hydrodynamic calculations were not able to describe momentum distribution, elliptic flow and observables of the HBT interferometry at the same time. One of the many ways how to solve it was Blast-wave model which is based on the hydrodynamic calculations aiming to describe the system at the freeze-out with a minimal set of paramaters.

Here we will use parametrization which was developed by Fabrice Retiere and Michael Annan Lisa [42]. This parameterization contains eight parameters T, ρ_0, ρ_2, R_y, R_x, a_s, τ_0 and $\Delta\tau$. The physical meaning of these parameters is given below.

The source is parametrized in the Cartesian coordinated system. The reaction plane is the (x-z) plane. In the beam (z) direction the freeze-out distribution is infinite and elliptical in the transverse (x-y) plane where the shape is controlled by the radii R_x

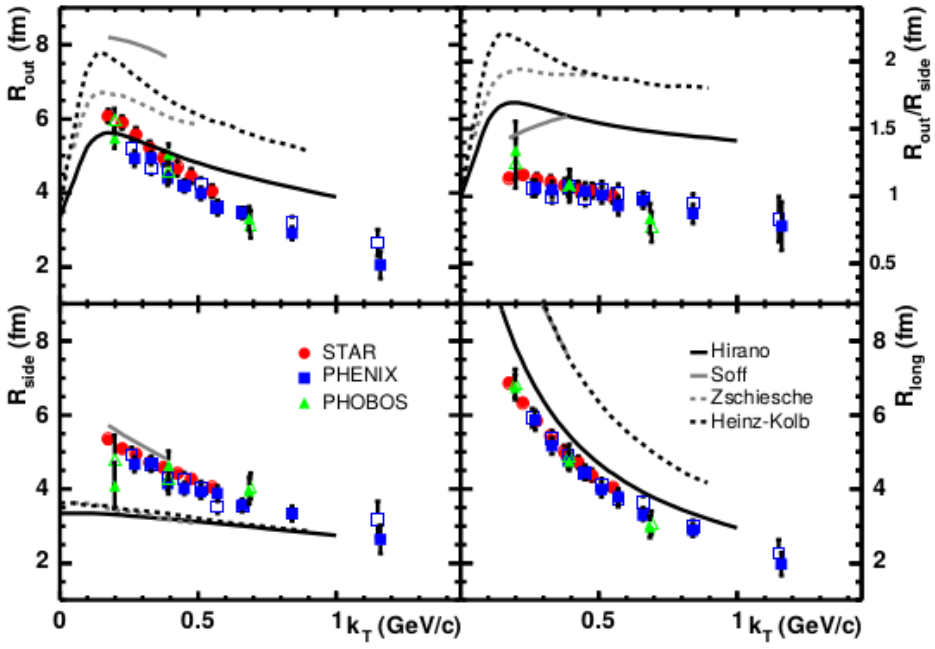

Figure 5.14: Hydrodynamic and hybrid hydrodynamic/cascade models calculations in comparison to RHIC data from Au+Au collisions at $\sqrt{s_{NN}} = 200\,GeV$. Open symbols represent data from π^-, π^- correlations and closed symbols for π^+, π^+ correlations. Taken from [34].

and R_y. The spatial weighting of source elements is given by

$$\Omega(r, \phi_s) = \Omega(\tilde{r}) = \frac{1}{1 + e^{(\tilde{r}-1)/a_s}} \tag{5.43}$$

where ϕ_s is the aimuthal angle of the source element and a fixed value of the normalized elliptical radius

$$\tilde{r}(r, \phi_s) = \sqrt{\frac{(r\ cos(\phi_s))^2}{R_x^2} + \frac{(r\ sin(\phi_s))^2}{R_y^2}} \tag{5.44}$$

corresponds to a given elliptical sub-shell within the solid volume of the freeze-out distribution. The parameter a_s corresponds to a surface diffuseness of the emission source. When $a_s = 0$, there is a hard edge, while $a_s \approx 0.3$ the profile is a Gaussian shape. This parameter is usually set to 0 for simplicity, see (Fig. 5.15).

A global temperature T is used to describe the spectrum of particles emitted from source element at each point (x, y, z). This element is also boosted by a transverse rapidity $\rho(x, y)$. This boost is perpendicular to the elliptical sub-shell of the source element profile, see (Fig. 5.16). Thus one can show that

$$tan(\phi_s) = (\frac{R_y}{R_x})^2 tan(\phi_b) \tag{5.45}$$

where ϕ_b is the azimuthal angle of the source velocity. For central collisions the flow

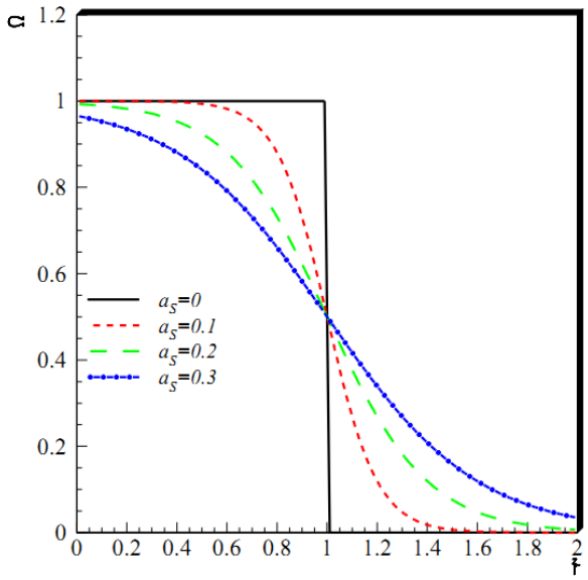

Figure 5.15: The source weighting function Ω versus normalized elliptical radius $\tilde{r}$. The surface diffuseness parameter is changed for several values. Taken from [42].

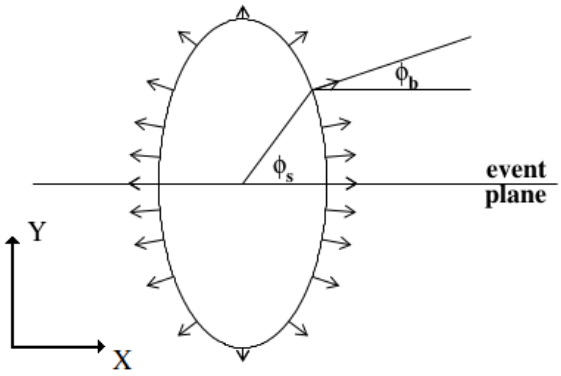

Figure 5.16: Schematic illustration of an elliptical sub-shell of the source. Here the source is extended out of the reaction plane $R_x < R_y$. Taken from [42].

rapidity bost strength depends linearly on the normalized elliptical radius $\tilde{r}$. Thus, in absence of an azimuthal dependence of the flow all source elements on the outer edge of the source boost with the same transverse rapidity ρ_0 in an outward direction. For non-central collisions, the flow rapidity is given by adding a parameter rho_2 which characterizes the strength to the second order. Hence the flow rapidity is given as follow

$$\rho(\tilde{r}, \phi_s) = \tilde{r}(\rho_0 + \rho_2 cos(2\phi_b)). \tag{5.46}$$

The source anisotropy enters into our parametrization in two independent ways and each affects elliptic flow. The first, setting $\rho_2 > 0$ means the boost is stronger in-plane than out-plane. The second way is to set $R_y > R_x$ for $\rho_0 \neq 0$ but $\rho_2 = 0$. This case also generates positive elliptic flow because there are more sources emitting in-plane

than out-plane.

There is a assumption that this model is longitudinally boost-invariant. The assumption is sensitive that the freeze-out accurs with a distribution in longitudinal proper time $\tau = \sqrt{t^2 - z^2}$. The model assume a Gaussian distribution peaked at τ_0 with the width $\Delta\tau$ as follow

$$\frac{dN}{d\tau} \sim exp(-\frac{(\tau - \tau_0)^2}{2\Delta\tau^2}). \tag{5.47}$$

We note that although the source emits particles over a finite duration in proper time τ , we assume that none of the source parameters changes with τ because calculation of the time dependence of these parameters requires a true dynamical model which is outside of this thesis.

The emission function of this model has a follow form

$$S(x,K) = m_T cosh(\eta - Y)\Omega(r,\phi_s) e^{\frac{-(\tau-\tau_0)^2}{2\Delta\tau^2} \sum_{n=1}^{\infty} (\pm)^{n+1} e^{-nK\cdot u/T}}, \tag{5.48}$$

where upper (lower) sign is for bosons (fermions). he reduction of the sum to the first term will transform the model to Boltzmann thermal distribution. After some steps which can be wieved in [42] the emission function can be rewritten as follow

$$S(x,K) = m_T cosh(\eta - Y)\Omega(r,\phi_s) e^{\frac{-(\tau-\tau_0)^2}{2\Delta\tau^2} \sum_{n=1}^{\infty} (\pm)^{n+1} e^{n\alpha cos(\phi_b - \phi_p)} e^{-n\beta cosh(\eta - Y)}}, \tag{5.49}$$

where we define

$$\alpha = \frac{p_T}{T} sinh[\rho(r,\phi_s)] \tag{5.50}$$

$$\beta = \frac{m_T}{T} cosh[\rho(r,\phi_s)] \tag{5.51}$$

. One can simplify the equation by setting $Y = 0$. Also, we introduce a function

$$\left\{B'\right\}(K) = \sum_{n=1}^{\infty} \left\{ (\pm)^{n+1} \int_0^{2\pi} d\phi_s \int_0^{\infty} r dr [2K_1(n\beta) B'(x,K) e^{n\alpha cos(\phi_b - \phi_p)} \Omega(r,\phi_s)] \right\}. \tag{5.52}$$

Then, p_T spectrum can be calculated as follow

$$\frac{dN}{p_T dp_T} = \int d\phi_p \int d^4x \; S(x,K) \propto m_T \int d\phi_p \{1\}(K) \tag{5.53}$$

and v_2 is calculated as

$$v_2(p_T, m) = \frac{\int_0^{2\pi} d\phi_p \{cos(2\phi_p)\}(K)}{\int_0^{2\pi} d\phi_p \{1\}(K)}. \tag{5.54}$$

For us the most important conclusion from the work of Retiere and Lisa are HBT radii and their dependence on the parameterization of the source. Using this parameterization one can obtain that R_l^2 carries information about the lifetime of the source and can be parametrized as follow

$$R_l^2(m_T) = \tau_0^2 \frac{T}{m_T} \frac{K_2(m_T/T)}{K_1(m_T/T)}. \tag{5.55}$$

and that this equation coincides with equation 5.38 from work [48].It is possible to show that the R_s^2 contains only spacial information and the R_o^2 is sensitive to the temporal extents of the source than the dynamical properties of the measured system can be described by the ratio of R_o^2 and R_s^2 as well as the difference of R_o^2 and R_s^2. For more detailed analysis we recommend to read [42].

5.5 Experimental approach

In order to obtain the HBT radii from experiment, we have to fit the experimentally measured correlation function by fitting function. The correlation function is defined as follow

$$C(\vec{q}, \vec{k}) = \frac{A(\vec{q})}{B(\vec{q})}, \tag{5.56}$$

where $A(q)$ is the pair distribution with relative momentum $\vec{q}$ in the same event (real pairs) while $B(q)$ is the pair distribution with relative momentum $\vec{q}$ in the different events (mixed pairs). Mixed pairs are made by event mixing technique. Here we select several different events with similar global variables and then particle pairs are made by choosing one particle from a event and choosing one particle from other event. Therefore the mixed pairs does not include the HBT effect, while the real pairs, from the same events, includes the HBT effect and interactions.

Chapter 6

Data analysis

In this work, we present the femtoscopy correlation of positive pions for p+Au collisions. The following sebsections describe the analysis procedure where the data set, event selection, track selection and pion identification are deal.

6.1 Data set

Our analyzed data originate from p+Au collisions at $\sqrt{s_{NN}} = 200\,GeV$ taken at the STAR experiment at RHIC in 2015 (Run 15) which include daynumbers from 124 to 159 with a minimum bias trigger using the BBC and VPD detectors.

1. Production: P16id
2. Library: SL14g
3. Trigger: BBCMB, VPDMB-novtx, VPDMB-30
4. Offline Trigger ID: 500008, 500018, 500004, 500904
5. FileCatalog command: catalog:star.bnl.gov?production=P16id, trgsetupname=production_pAu200_2015,filetype=daq_reco_MuDst, daynumber[]124-159, filenamest_physics,collision=pAu200,sanity=1,available=1, tpx=1,tof=1,storage!=HPSS"preferStorage="local" nFiles="all"
6. Total number of events: 3.77 billions
7. Number of events using triggers: $\sim$ 130M

When total events pass through the system one obtains $\sim$ 130M events and then event cuts can be applied to this event cuts.

6.2 Event selection

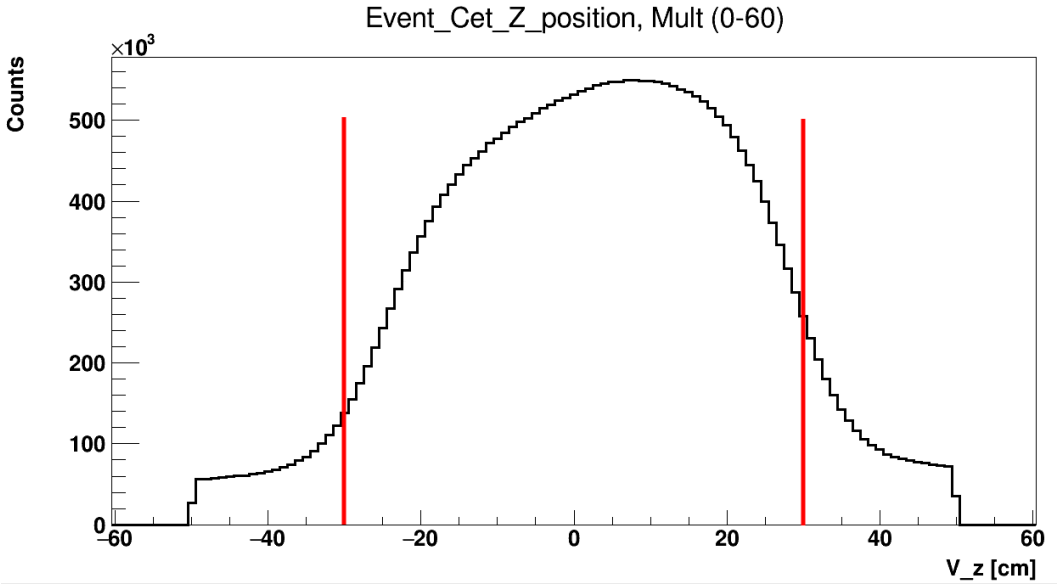

Figure 6.1: The distribution of the z-coordinate of the primary vertex position for $\mid V_z \mid < 30\,cm$.

For our analysis the selection of events in the center of the TPC is required, then a cut on the position of the primary vertex along the beam direction (z-axis) was applied. Our requirement for this cut is $\mid V_z \mid < 30\,cm$, there V_z is the z-coordinate of the primary vertex position which is measured by the TPC, see in (Fig.6.1), tails of the histogram for primary vertex in z-direction do not contain enough counts and therefore they are not added into analysis. It is known that V_z can also be calculated by the VPD detectors. Therefore there is also another requirement, using a difference between the vertex position measured by the TPC and VPD detectors in an absolute value was less than $5\,cm$. To remove pile-ups and badly detected events.

Event Multiplicity

In our analysis the reference multiplicity was used. Usually, thanks to models we are able to calculate centrality bins for the corresponding multiplicity however, in the case of $p-Au$ collisions a relevant model is not known. Therefore we have divided reference multiplicity into the four intervals as can be seen in (Fig.6.2). For these multiplicity bins we will construct correlation functions, see results. It was mentioned in previous chapter, (4.5 Experimental approach), that the denominator of the experimental correlation function, (Eq. 4.56), is formed by mixing particles from one event with all particles from similar events in order to avoid any signal in the correlation function that could be produced by mixing events with different characteristics. Therefore, in our analysis, similar events are done according the position of the z-coordinate of the

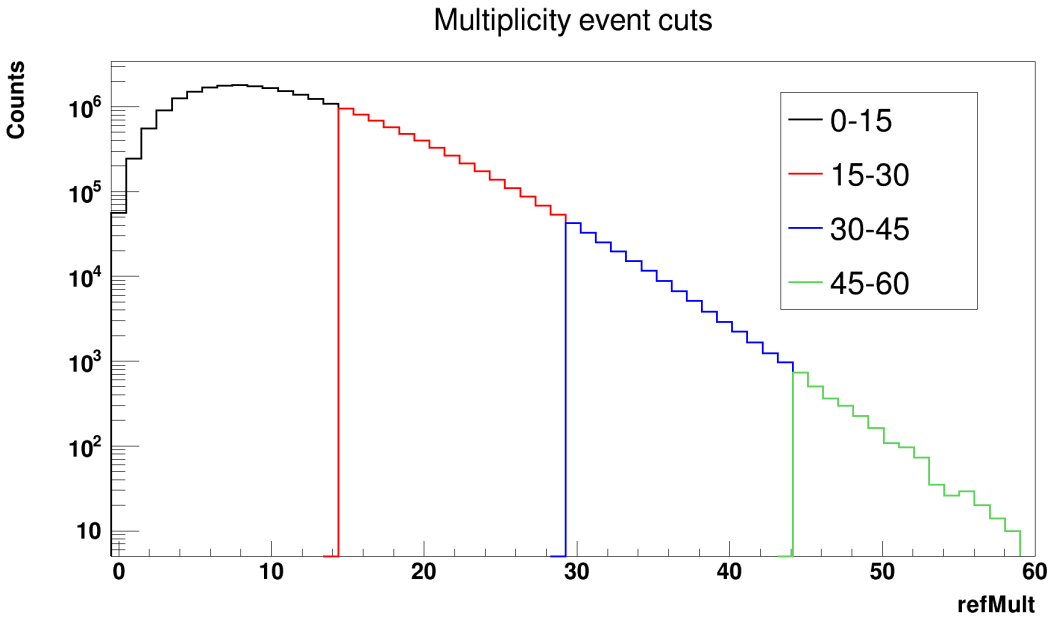

Figure 6.2: Distribution of the reference multiplicity for p-Au collisions divided into the five bins.

primary vertex and uncorelated multiplicity. In our case primary vertex position is within 30 cm for four multiplicity bins.

6.3 Particle selection

Particle identification was done by the TPC and ToF detectors. In the TPC, this identification is based on the energy losses of the particles, which travel through a gas inside the detector. This losses depend on the velocities at which particles travel in the TPC. It means that for a given momentum, three particles with different masses have different velocities and thus they have different dE/dx, see in (Fig.6.3). As was mentioned in Chapter 3 (3.2.1 TPC detector), energy losses of charged particles by ionization are calculated using the Bethe-Bloch formula, see (Eq.3.1). For us, the positive charged pions are important but it can be seen that for high momentum there is some contamination from other particles which is going to effect $\lambda(\vec{k})$ parameter. In order to solve this contamination problem we also apply a cut on mass squared.

In analysis presented here, there is specific p_T cut which was applied to single tracks because the TPC enables to identify particles with the transverse momentum larger than 0.15 GeV/c. Moreover, we also applied another cut for momentum of single particles due to limitations in the identification of pions due to mixing of the dE/dx bands at high momentum, see (Fig.6.3). Therefor, only tracks with $(0.15 < p_T < 1.5 GeV/c)$ and $(0.15 < p < 1.5\, GeV/c)$ are included in the correlation functions. In addition to make sure that emitted particles fall into the detector acceptance there is

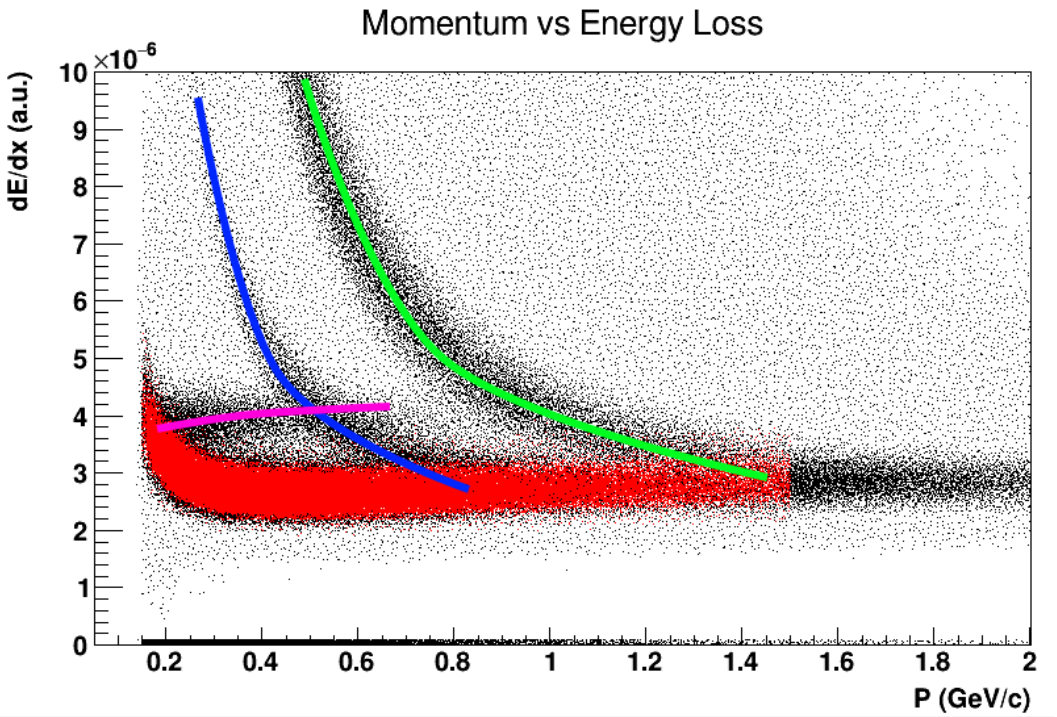

Figure 6.3: dE/dx vs. momentum of the particles for pions (red), kaons (blue) and protons (green) and elentrons (pink).

a requirement for primary tracks to be in a pseudorapidity range $\mid \eta \mid < 1$.

However, as we mentioned the pion band is contaminated by the kaon and proton and therefore we do not obtain only pions. In order to ged rid of the kaons and protons the ToF detector was used. This detector measures the time of flight β. When this information is combined with the measured momentum in TPC, the particle mass m can be calculated by (Eq. 3.5). The ToF enables to separate charged pions from kaons and protons up to $1.5\,GeV/c$. Therefore, the last identification cut requires the track to have the mass squared in the range $0.005 < m^2 < 0.035$, see (Fig.6.4).

6.4 Pair cut

Since this is a preliminary work we will not discuss cuts that are intended to remove the effects of two track reconstruction defects that have high impact on HBT. The mentioned effects are

- Splitted tracks: one single particle reconstructed as two tracks
- Marged tracks: two particles with similar momenta reconstructed as one track

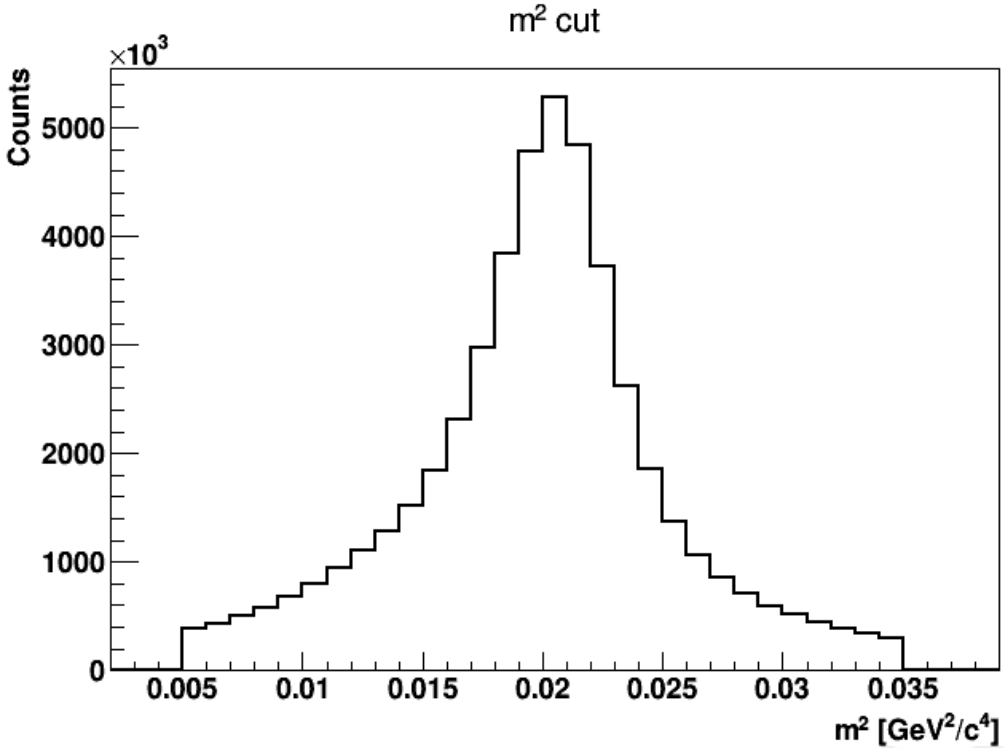

Figure 6.4: The distribution of the mass squared of positively charged pions which was determined by the TPC and ToF detectors.

k_T cuts

The only cut which will be apply to pairs will be tranverse momentum (k_T) cut. As was already discussed, homogeneity regions are expected to depend on the pair transverse momentum. Hence such cut enables to change the size of the measured volume at the constant centrality and temperature of the system. Our requirement for this cut is to have an average value between $0 < k_T < 1.5\,GeV/c$. This range was divided into five bins: 0.0-0.3, 0.3-0.6, 0.6-0.9, 0.9-1.2, 1.2-1.5 GeV/c.

An example of one-dimensional correlation functions for selected data are shown in (Fiq.6.5 and Fiq.6.6). Here, one can see a typical shape of the correlation function. For small values of q_{inv} the Coulomb interacion can be watched. As can be seen in (Fig.6.5), with increasing the multiplicity the correlation function decreases and it means that radius of the homogeneity region increases, see in (Fig.7.2). In (Fig.6.6) we can see that with increasing of k_T the correlation function also increases and that means that radius of homogeneity region decreases. This corresponds with predicion from chapter 4 (4.4 Femtoscopy and dynamical system) and also with our results (Fig.7.2).

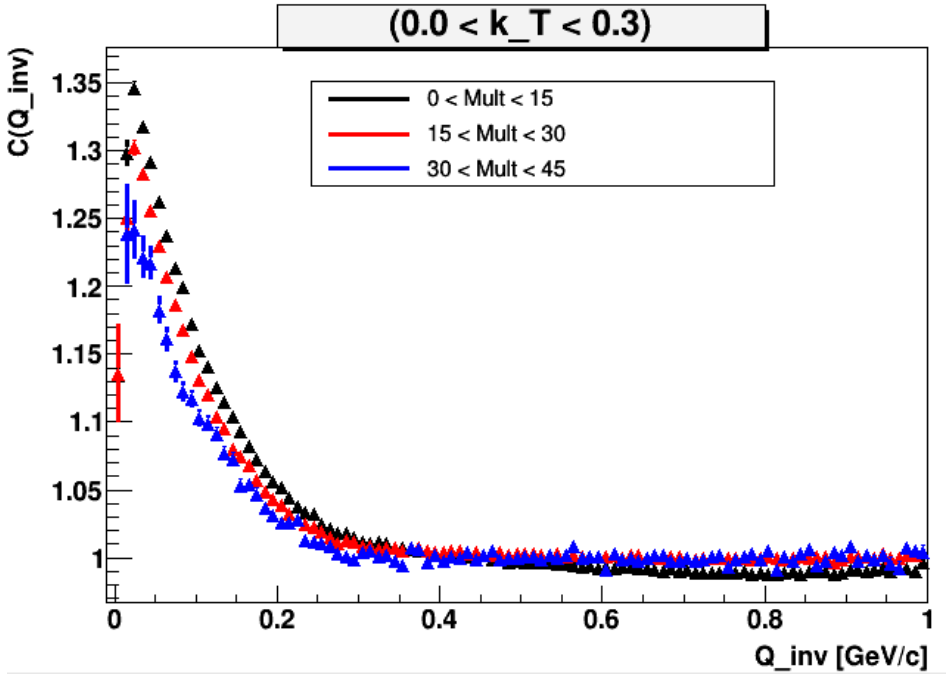

Figure 6.5: One dimensional correlation functions for 3 multiplicity ranges and $0.0 < k_T < 0.3$.

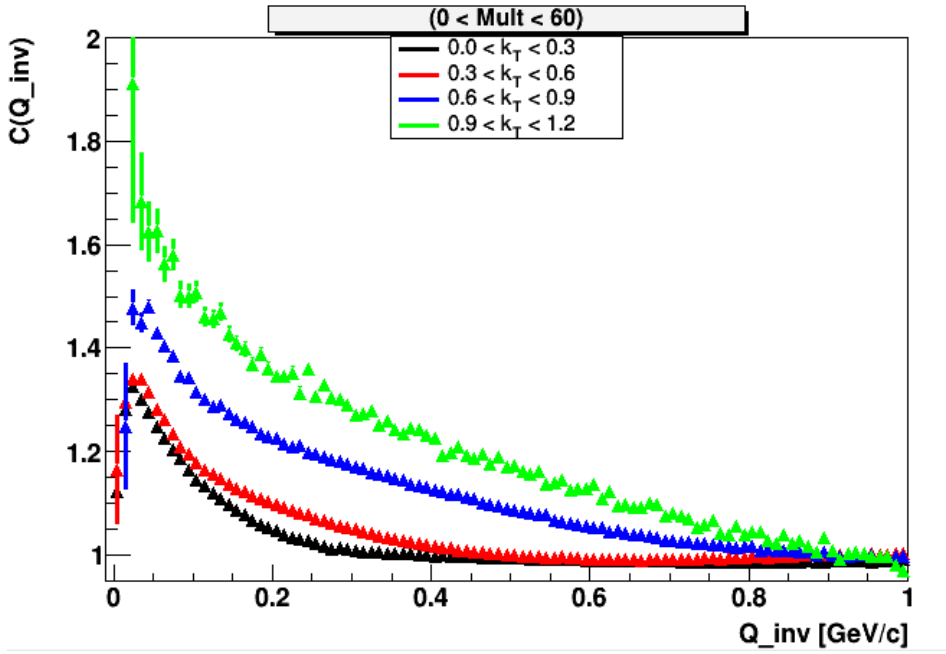

Figure 6.6: One dimensional correlation functions fot positive pions for multiplicity range 0-60 and for 4 k_T bins

Chapter 7

Results

In the previous chapter the data, which were used for a construction of the correlation function, were analysed. In this chapter our experimental correlation functions for the positive charged pions are studied in detail. Here we have to mention that we will not consider track splitting and merging, purity and momentum correction or pile-up. All these things can modify our correlation function however, for the purpose of the preliminary analysis these corrections have to not be considered. The functions are fitted with two simple models and are compared with other experimental correlation functions from different experiments. In our analysis we will not consider and fit the Coulomb part of the correlation function due to difficulty of fitting this area.

7.1 1D-Correlation function

The one-dimensional uncorrected correlation functions for Bose-Einstein correlation (no FSI) are fitted by

$$\begin{aligned} C_{Gauss}(\vec{q},\vec{k}) &= 1+\lambda(\vec{k})e^{-(q_{inv}R_{inv}(\vec{k}))^2} \\ C_{Levy}(\vec{q},\vec{k}) &= 1+\lambda(\vec{k})e^{-|q_{inv}R_L(\vec{k})|^{\alpha}}. \end{aligned} \tag{7.1}$$

The first equation is well known Gaussian distribution, here q_{inv} is the Lorentz invariant momentum defined in (Eq. 4.21), R_{inv} is the Lorentz invariant radius and λ is the chaoticity parameter. The second equation is the Levy distribution, here q_{inv}, R_L and λ have the same meaning as in the case of the Gaussian distribution but α is the Levy index called also index of stability, which can be equal to the values $0 < \alpha \leq 2$. There are two specific case, at $\alpha = 2$; the Gaussian parametrization corresponded to the normal (Gaussian) distribution function

$$S_{\vec{k}}(\vec{x}) = \frac{1}{\sqrt{2\pi R_G^2}} e^{-\frac{(x-x_0)^2}{2R_G^2}}, \tag{7.2}$$

where the Gaussian scale parameter is $R_G^2 = \langle x^2 \rangle - x_0^2$, the standart deviation. Another specific case of the Levy distribution is at $\alpha = 1$ which is called exponential parametrization and it corresponds to the Cauche (Lorentzian) distribution function

$$S_{\vec{k}}(\vec{x}) = \frac{R_c}{\pi(R_c^2 + (x - x_0)^2)}, \tag{7.3}$$

with scale parameter R_c. For more details about Levy distribution see [39].

Figures (Fig.7.3 - Fig.7.6) show examples of one-dimensional correlation functions for different reference multiplicity ranges: 0-60, 0-15, 15-30, 30-45, 45-60, respectively. In each multiplicity range, k_T is divided into five bins as was mentioned previous. Due to poor statistic we have not considered and described correlation functions for multiplicity bins 45-60.

One can see that fits do not include an area where the Coulomb interaction has a significant influence, (small q_{inv}). In order to fit this data with the Coulomb interaction one has to use different models unlike (Eq.7.1) but this is not the main idea of this work. As can be seen from comparison of the fits, almost in all cases the Levy fits better describe data than the Gaussian fits which means that the source is of non-Gaussian shape. In the figures we can also see χ^2 however, in our cases this test is not very useful because as can be seen fits do not do not describe data properly.

Results from fits of correlation functions for different multiplicities and k_T bins are presented in (Fiq.7.1 and Fig.7.2). Here the λ parameter and source radius R_{inv} and R_L are shown as a function of the multiplicity and pair transverse momentum k_T.

As we mentioned, the source radii R decrease with the pair tranverse momentum k_T for the Levy distribution as well as for the Gaussian distribution. This behaviour qualitatively agrees with the effect expected from a system undergoing a transverse expansion where pairs with the larger transverse momentum are emitted from a smaller homogeneity region than the pairs with the smaller k_T, as it was discussed in Chapter 4. A dependence of the radii R_{inv} and R_L on the multiplicity is already not such clear. One would expect that with higher multiplicity the radii of the homogeneity region increase however it is hard to confirm this fact from the (Fig.7.2). As we can see, for the Gauss radii this dependence can be observed in a range of errors but for the Levy radii such a behaviour is not observed. For this observation a more precise analysis must be done.

The behaviour of the λ parameter is not monotonic. In the case of Levy distribution, for small multiplicities this parameter decreases for lower k_T bins and then increases while for bigger multiplicities it is almost constant for lower k_T bins and then it increases. For Gaussian distribution this parameter decreases very weakly, it is almost constant for lower k_T bins but then it increases too.

For completeness, the behaviour of levy parameter (α) is pltted in (Fig.7.3-Fig.7.6) on the left side down. We can see that the parameter complies with the condition

$0 < \alpha \leq 2$. For a comparison, in (Fig.7.7) we present STAR preliminary analysis for $Au + Au$ collisions at $200\,GeV$ for centrality range 0-5% and for eight k_T bins [14]. One can see that a magnitude of the correlation functions is less than in our case. This agrees with a fact that for a bigger source the correlation is weaker. One can also compare that with higher k_T the magnitude of the correlation increases, this corresponds with a fact that for higher k_T the homogeneity region is smaller and for smaller homogeneity region the correlation is bigger. In (Fig.7.8) is shown a dependence of the λ parameter and radius on k_T. Here we see that behaviour is completely different as in our case.

(Fig.7.9) shows three $\pi\pi$ correlation functions versus q_{inv} for $p + p$, $d + Au$ and $Au + Au$ that have not been Coulomb corrected. As the system size decreases from $Au + Au$ to $p + p$, the width of the correlation function increases. Note that Bose-Einstein correlations are not a small effect in $d + Au$ or $p + p$ collisions in comparison to $Au + Au$.

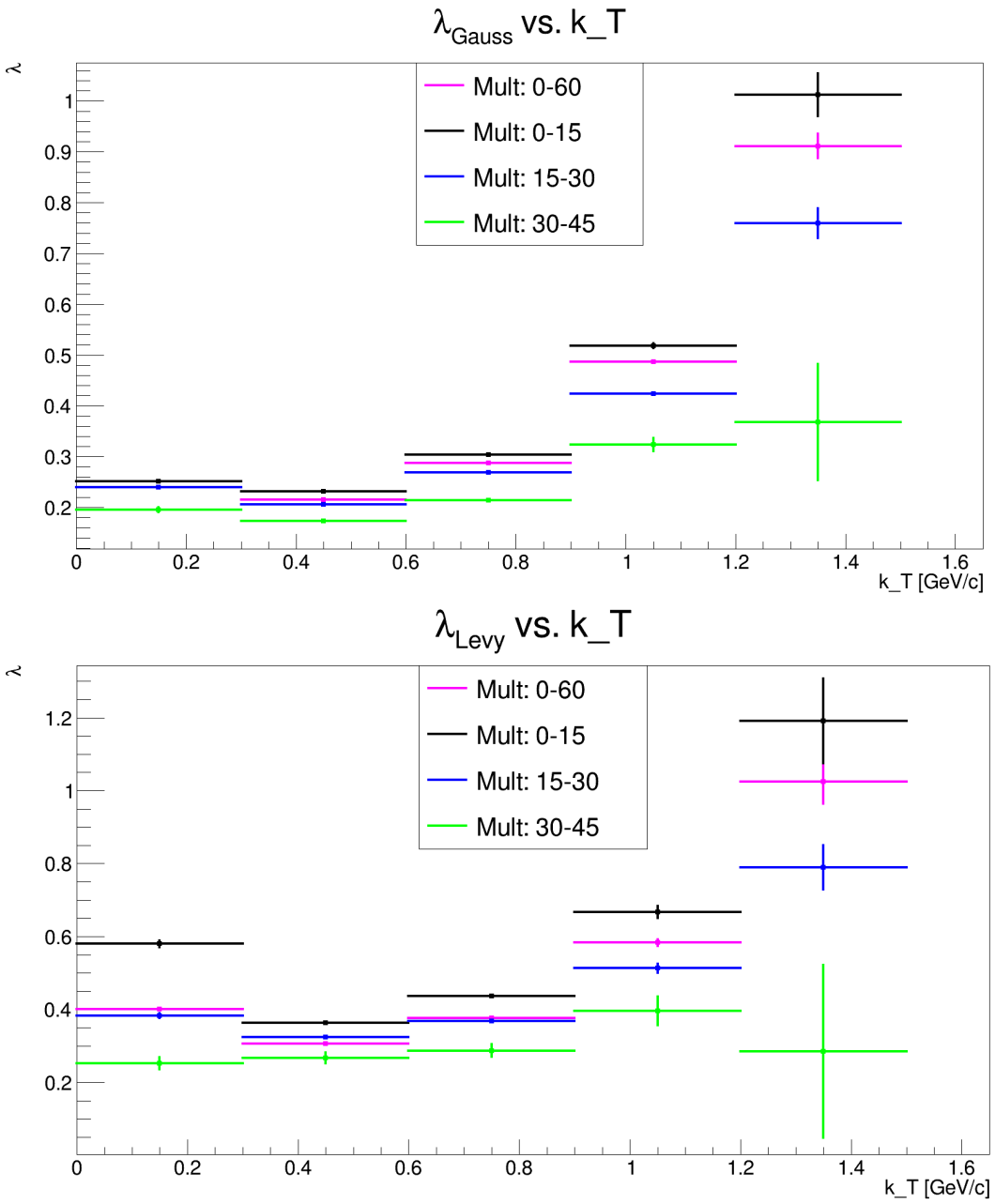

Figure 7.1: Fit results: λ as a function of k_T and multiplicity. Top panel is for Gaussian distribution. Bottom panel is for Levy distribution.

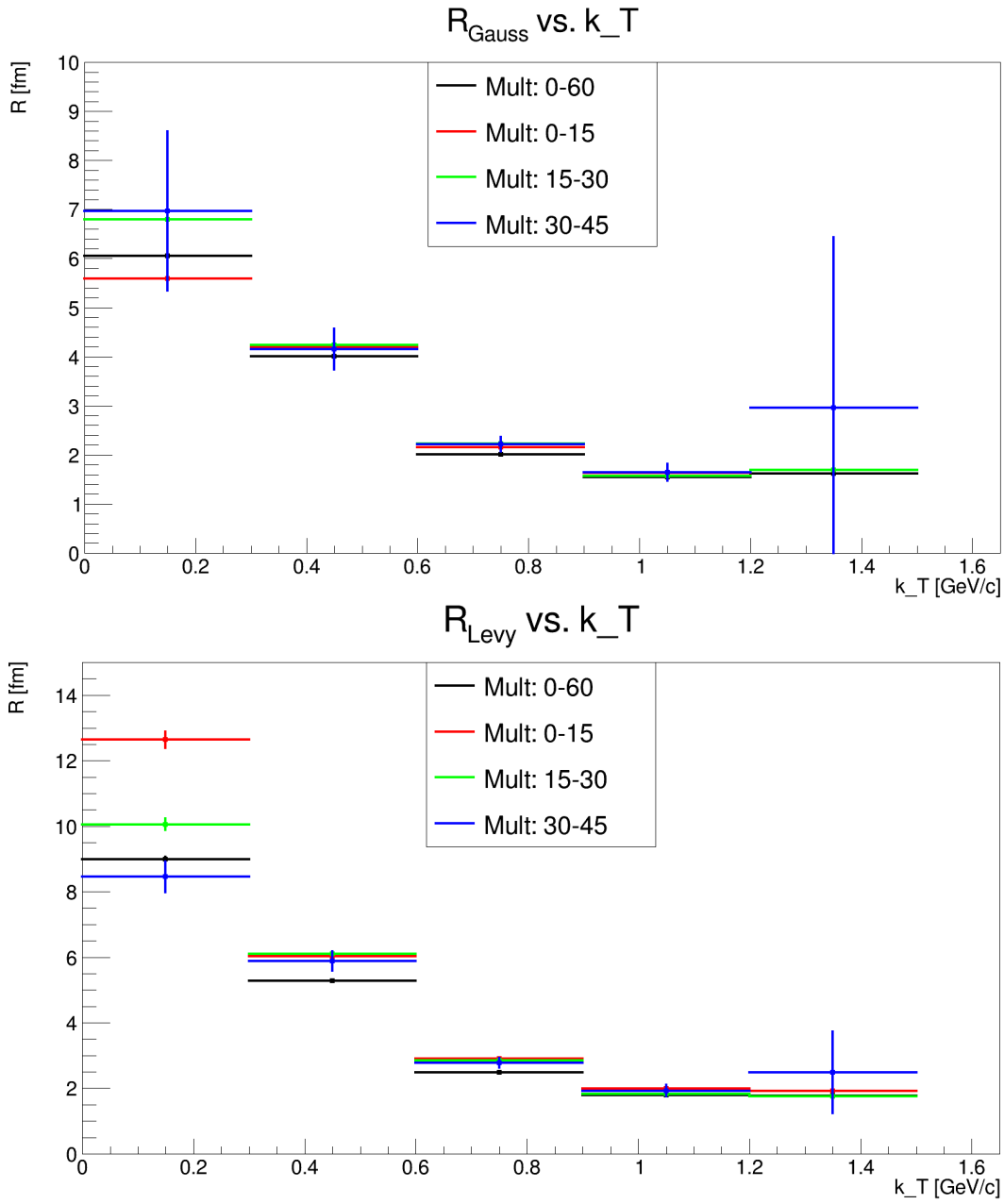

Figure 7.2: Fit results: R_{inv} and R_L as a function of k_T and multiplicity. Top panel is for Gaussian distribution. Bottom panel is for Levy distribution.

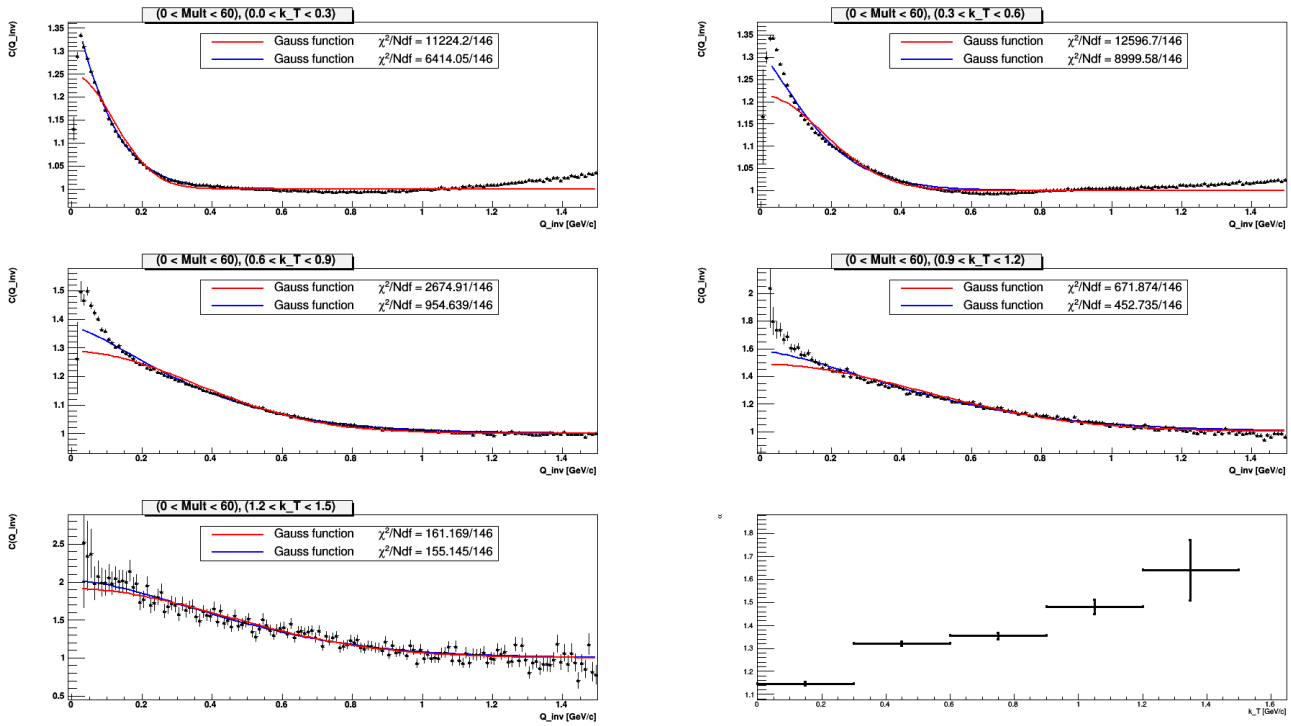

Figure 7.3: One-dimensional correlation function for positive pions for multiplicity 0-60 and five k_T bins. The lines represent fits to the data by using (Eq.7.1). On the left side down is plotted dependence of levy parameter (α) as a function of k_T.

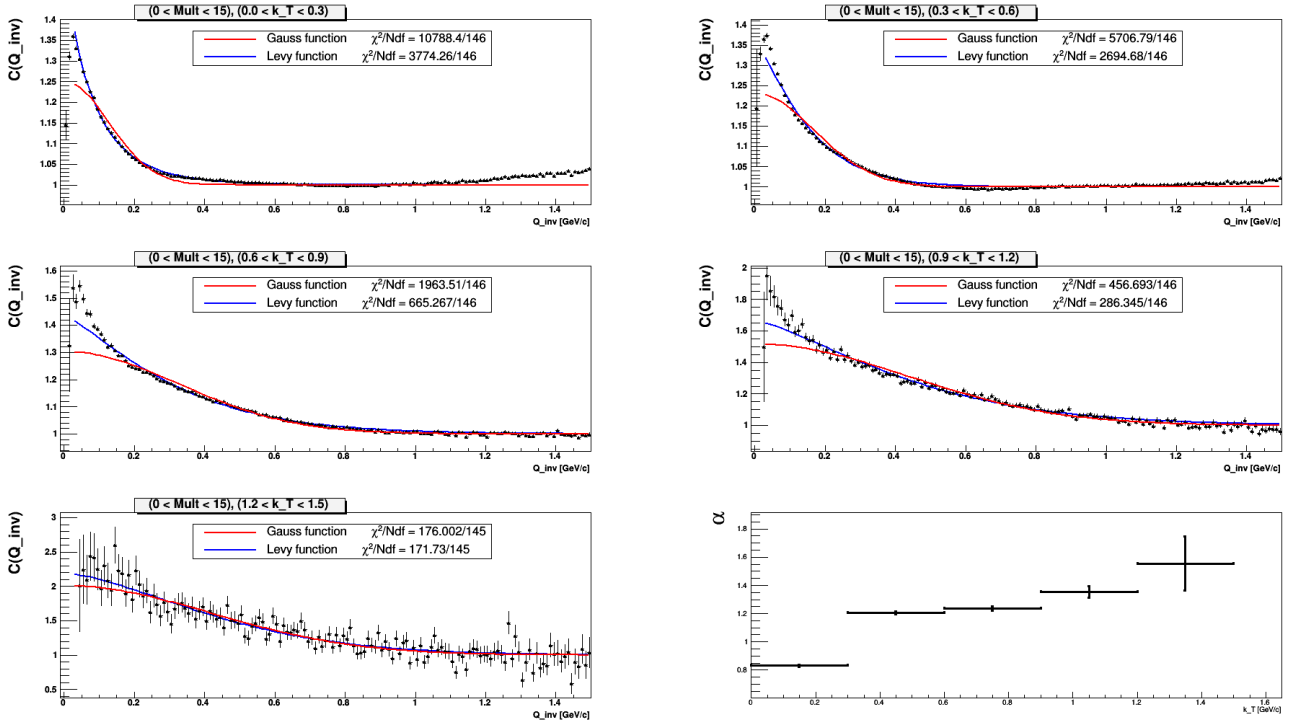

Figure 7.4: One-dimensional correlation function for positive pions for multiplicity 0-15 and five k_T bins. The lines represent fits to the data by using (Eq.7.1). On the left side down is plotted dependence of levy parameter (α) as a function of k_T.

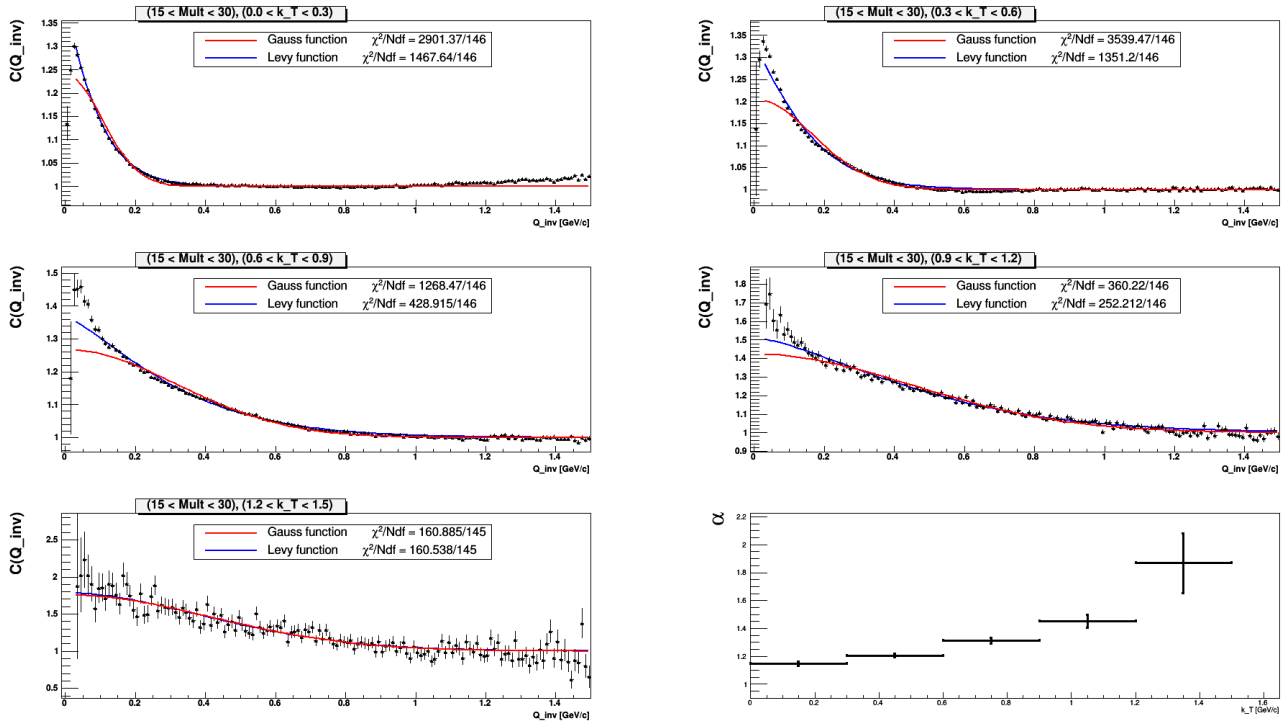

Figure 7.5: One-dimensional correlation function for positive pions for multiplicity 15-30 and five k_T bins. The lines represent fits to the data by using (Eq.7.1). On the left side down is plotted dependence of levy parameter (α) as a function of k_T.

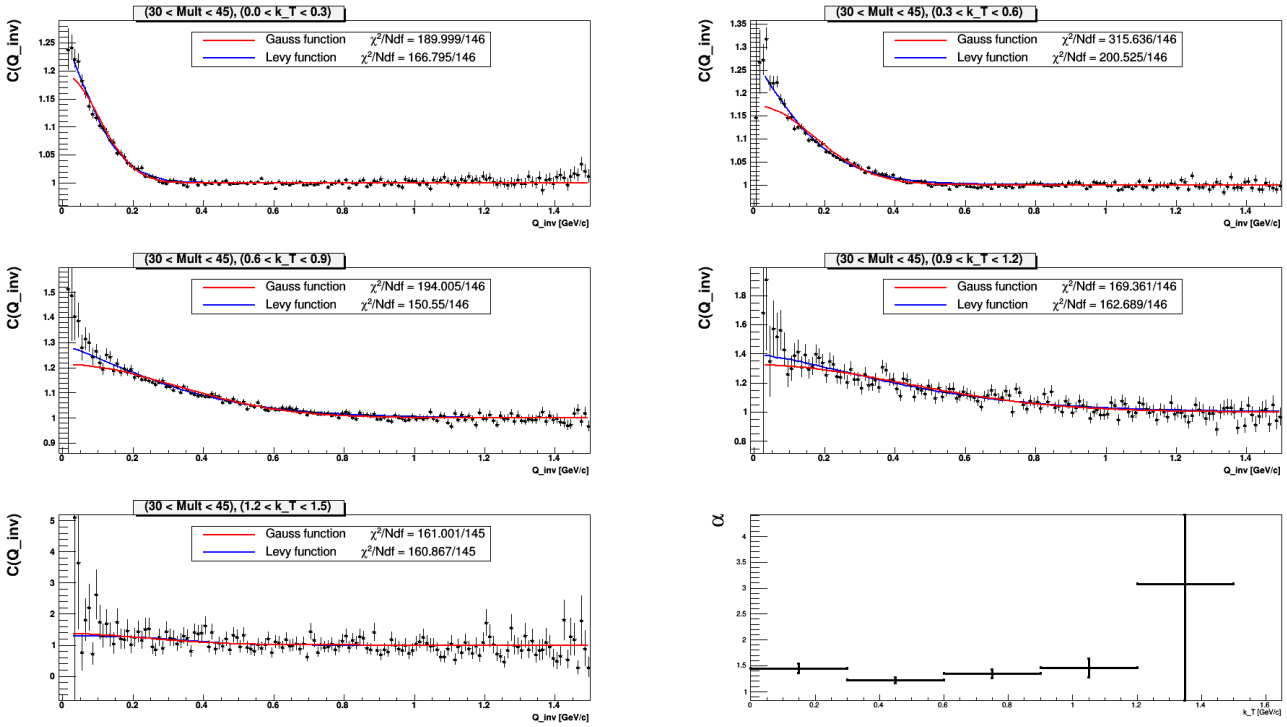

Figure 7.6: One-dimensional correlation function for positive pions for multiplicity 30-45 and five k_T bins. The lines represent fits to the data by using (Eq.7.1). On the left side down is plotted dependence of levy parameter (α) as a function of k_T.

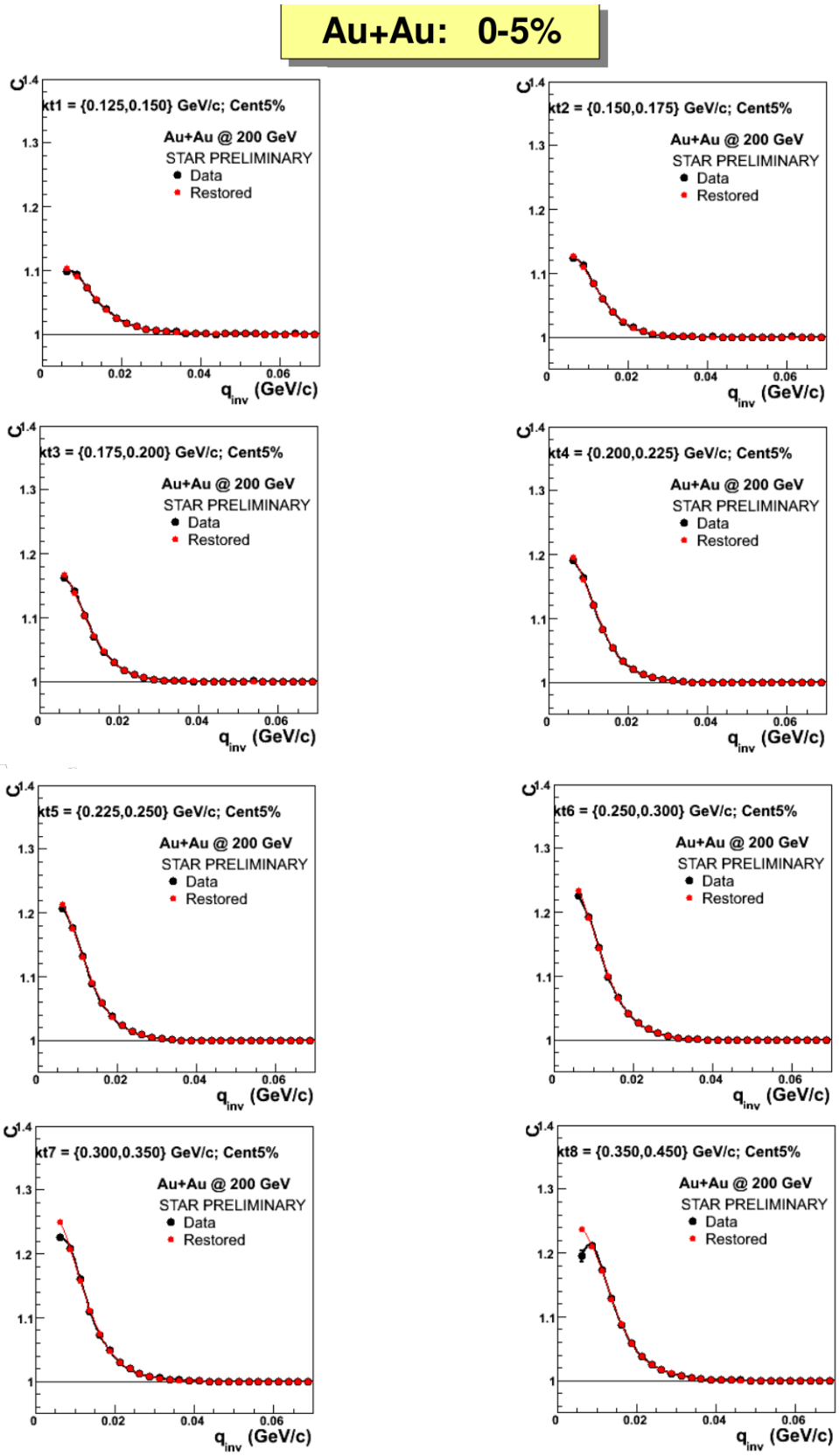

Figure 7.7: One-dimensional correlation functions for pions for centrality 0-5% and eight k_T bins. Taken from [14]

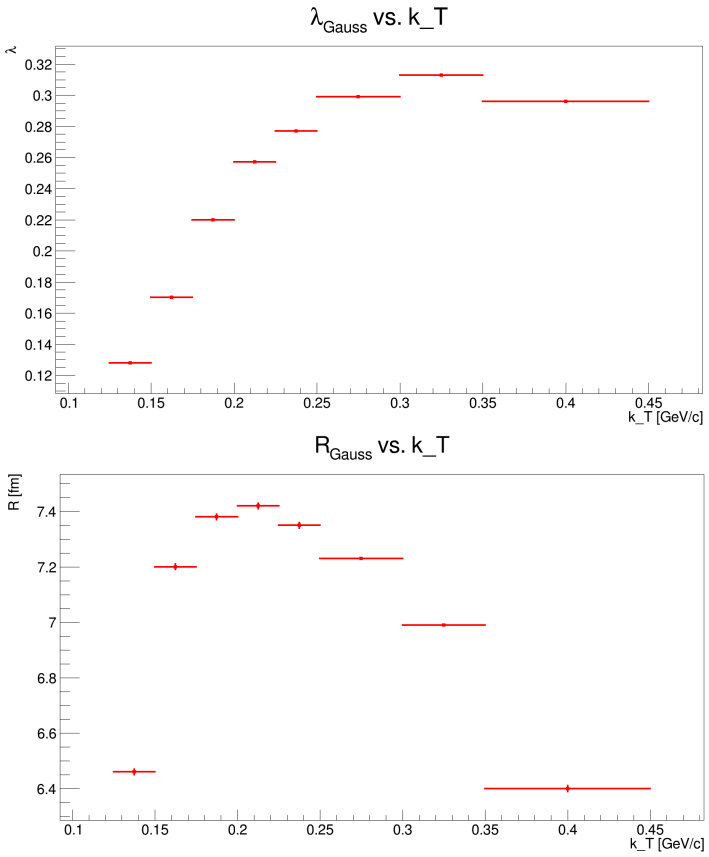

Figure 7.8: Top panel: dependence of λ parameter on k_T. Bottom panel: dependence of R_{inv} on k_T. Taken from [14]

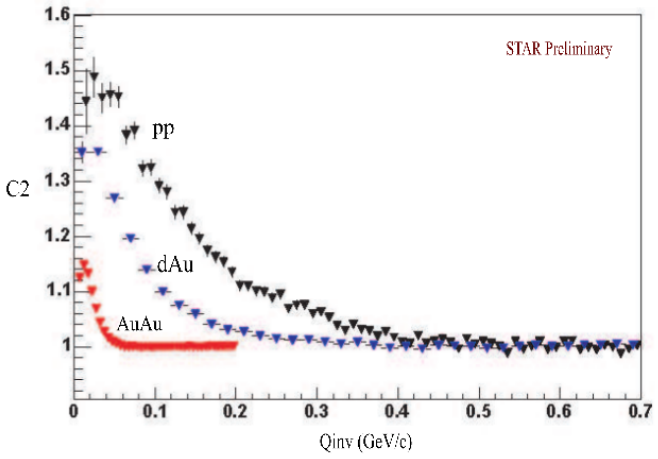

Figure 7.9: Typical one-dimensional $\pi\pi$ correlation functions for the $p+p$, $d+Au$ and $Au+Au$ systems at STAR. The $p+p$ and $d+Au$ correlation functions are from minimum bias data while the correlation function from $Au+Au$ is shown for central collisions at $\sqrt{s} = 200\,GeV$. All are subject to the same k_T cut. Taken from [28].

Chapter 8

Conclusion

The main goal of this work was to present a preliminary analysis of the femtoscopic study of two-particle correlation function for positive charged pions. The presented analysis was performed on a minimum bias data from $p - Au$ collisions at $\sqrt{s_{NN}} = 200\,GeV$ collected by the STAR experiment.

Applying the selected criteria, the one-dimensional correlation functions for pairs of positive pions were created, see (Fig.7.3-Fig.7.6). Functions were constructed for five multiplicity and five k_T bins. They were fitted by two simple models, Gaus and Levy functions.

For these models the graphs of λ parameter versus k_T, (Fig.7.1) and radius R_{inv} (R_L), (Fig.7.2) were created. From these figures one can see that there is a visible dependence of R_{inv}, R_L and λ parameters on multiplicity and k_T. In case of the Levy model, the dependence of λ on k_T for small values is different as in the case of Gauss model. For $k_T > 0.4\,GeV/c$ the λ parameter increases for both cases. However, dependence of these parameters on the multiplicity is very similar. Parameters λ with higher multiplicity are smaller than λ-s with smaller multiplicity for both cases.

In the case of radii, the behaviour for both cases is similar for k_T. When the pair momentum increases the radii decrease, as one can expect. However, multiplicity dependence for these radii is not as unambiguous as in the case of the pair momentum. For better results in that case we need a more precise analysis.

In (Fig.7.3 - Fig.7.6), on the left and down, the plots for levy parameter (α) were created. Almost in all cases the condition ($0 < \alpha \leq 2$) is satisfied and for all cases this parameter increases.

Comparing obtained data from our analysis for $p - Au$ with results from $Au - Au$ we can see that there are no similarities in radii or λ parameter. To obtain a better comparison one needs to do more precise analysis which will include some corrections and limits which improve selected data from which the correlation functions are constructed.

Bibliography

[1] A Modern Indroduction to Nuclear Physics. http://www.physics.umd.edu/courses/Phys741/xji/chapter1.pdf. Accessed: 2017-04-4.

[2] Asymptotic Freedom and the Coupling Constant of QCD. http://backreaction.blogspot.cz/2007/12/asymptotic-freedom-and-coupling.html. Accessed: 2017-04-3.

[3] Brookhaven National Laboratory. Laboratory, brookhaven national. http://www.star.bnl.gov. Accessed: 2017-04-23.

[4] Conceptual design report. https://drupal.star.bnl.gov/STAR/files/StarCDR.pdf. Accessed: 2017-04-23.

[5] Evolution of collisions and QGP. https://particlesandfriends.wordpress.com/2016/10/14/evolution-of-collisions-and-qgp/. Accessed: 2017-04-10.

[6] Experimental test of Asymptotic Freedom. arxiv.org/pdf/hep-ex/0606035. 2006-06-15.

[7] Fundamental Forces and Yukawa Theory. http://cronodon.com/Atomic/Fundamental_Forces.html. Accessed: 2017-04-1.

[8] How Low Can RHIC Go? https://www.bnl.gov/rhic/news2/news.asp?a=1870&t=today. Accessed: 2017-04-6.

[9] HTRA Galway. http://slideplayer.com/slide/4823367/. Accessed: 2017-07-12.

[10] Lectures on Quantum Chromodynamics. https://www.nikhef.nl/~h71/Lectures/2015/Other/qcdlecture.pdf. Accessed: 2017-04-3.

[11] Polarimetry. https://wiki.bnl.gov/rhicspin/Polarimetry. Accessed: 2017-04-15.

[12] Proposal for a Large Area Time of Flight System for STAR. https://www.star.bnl.gov/public/tof/publications/TOF_20040524.pdf. Accessed: 2017-04-25.

[13] Standart model. `http://www.eskesthai.com/search/label/Standard%20model`. Accessed: 2017-03-31.

[14] Twoparticle femtoscopy at STAR. `https://physics.fjfi.cvut.cz/cfrjs/minikonference/chaloupka_STAR_Femt.pdf`. Accessed: 2017-09-3.

[15] John Adams, Clemens Adler, MM Aggarwal, Z Ahammed, J Amonett, BD Anderson, M Anderson, D Arkhipkin, GS Averichev, SK Badyal, et al. Pion-kaon correlations in central a u+ a u collisions at s n n= 130 g e v. *Physical review letters*, 91(26):262302, 2003.

[16] John Adams, Clemens Adler, MM Aggarwal, Z Ahammed, J Amonett, BD Anderson, D Arkhipkin, GS Averichev, SK Badyal, J Balewski, et al. Azimuthally sensitive hanbury brown–twiss interferometry in a u+ a u collisions at s n n= 200 g e v. *Physical review letters*, 93(1):012301, 2004.

[17] Guido Altarelli and Theory Unit CERN, Department of Physics. Collider physics within the standard model: a primer. *arxiv.org/pdf/1303.2842.pdf*.

[18] Christopher Daniel Anson. *Energy dependent Hanbury Brown–Twiss interferometry and the freeze-out eccentricity of heavy ion collisions at STAR*. The Ohio State University, 2014.

[19] Rajeev S. Bhalerao. A viscous blast-wave model for relativistic heavy-ion collisions. *arXiv:1508.05878 [nucl-th]*.

[20] FS Bieser, HJ Crawford, J Engelage, Eppley, et al. The star trigger. *Nuclear Instruments and Methods in Physics Research Section A: Accelerators, Spectrometers, Detectors and Associated Equipment*, 499(2):766–777, 2003.

[21] G.E. Bruno. New results from the na57 experiment. *arXiv:nucl-ex/0403036*, 2004.

[22] M.N. Chernodub. Background magnetic field stabilizes qcd string against breaking. *arXiv:1001.0570 [hep-ph]*, 2010.

[23] ALICE Collaboration. Centrality determination of pb-pb collisions at $\sqrt{s_{NN}}$ = 2.76 tev with alice. *arXiv:1301.4361 [nucl-ex]*.

[24] S. S. Adler et al. Bose-einstein correlation of charged pion pairs in au+au collisions at s_{NN} = 200 gevs. *Phys. Rev. Lett. 93, 152302 (2004)*.

[25] S. S. Adler et al. Elliptic flow of identical hadrons in au+au collisions at s_{NN} = 200 gevs. *Phys. Rev. Lett. 91, 182301 (2003)*.

[26] S. S. Adler et al. Production of phi at midrapidity in at a center of mass energy per nucleon of 200 gev in au+au collisions at relativistic energies. *Phys. Rev. C72, 014903 (2005).*

[27] David J. Gross and Frank Wilczek. Ultraviolet behavior of non-abelian gauge theories. *Phys.Rev. Lett., 30:1343–1346*, 1973.

[28] Thomas D Gutierrez. Pion interferometry from pp and dau collisions at rhic. *arXiv preprint nucl-ex/0403012*, 2004.

[29] Brooke A. Haag. Characterization of au+au collisions at s_{NN} = 200 gev from star: from meson production in ultra-peripheral collisions to high-pt azimuthal correlations in central collisions. Dissertation thesis, Sonoma State University-2001, University of California at Davis-2003, 2009.

[30] Amaresh et al. Jaiswal. Relativistic heavy-ion collisions. *arXiv:1404.3294 [nucl-th].*

[31] Stanis law MRÓWCZYŃSKI. Quark-gluon plasma. *arXiv:nucl-th/9905005.*

[32] R Lednicky, S Panitkin, and Nu Xu. Search for delays between unlike particle emissions in relativistic heavy-ion collisions. *arXiv preprint nucl-th/0304062*, 2003.

[33] Jindřich Lidrych. Non-identical kaon femtoscopy at star experiment. diploma thesis, CZECH TECHNICAL UNIVERSITY IN PRAGUE, 2016.

[34] Michael Annan Lisa, Scott Pratt, Ron Soltz, and Urs Wiedemann. Femtoscopy in relativistic heavy ion collisions: two decades of progress. *Annu. Rev. Nucl. Part. Sci.*, 55:357–402, 2005.

[35] WJ Llope, F Geurts, Mitchell, et al. The tofp/pvpd time-of-flight system for star. *Nuclear Instruments and Methods in Physics Research Section A: Accelerators, Spectrometers, Detectors and Associated Equipment*, 522(3):252–273, 2004.

[36] Mercedes López Noriega. *Pion interferometry in AuAu collisions at a center of mass energy per nucleon of 200 GeV.* PhD thesis, The Ohio State University, 2004.

[37] W.Betts et al. M.Anderson, J.Berkowitz. The star time projection chamber: A unique tool for studying high multiplicity events at rhic2. *arXiv:nucl-ex/0301015.*

[38] Takafumi Niida. Measurements of quantum interference of two identical particles with respect to the event plane in au+au collisions at a center of mass energy of 200 gev at rhic-phenix. Dissertation thesis, University of Tsukuba, 2013.

[39] VA Okorokov. Lévy distributions for one-dimensional analysis of the bose–einstein correlations. *Advances in High Energy Physics*, 2017, 2017.

[40] Scott Pratt. The long slow death of the hbt puzzle. *Nuclear Physics A*, 830(1-4):51c–57c, 2009.

[41] Scott Pratt. Resolving the hanbury brown–twiss puzzle in relativistic heavy ion collisions. *Physical review letters*, 102(23):232301, 2009.

[42] Fabrice Retiere and Michael Annan Lisa. Observable implications of geometrical and dynamical aspects of freeze-out in heavy ion collisions. *Physical Review C*, 70(4):044907, 2004.

[43] Markus H. Thoma Thomas Peitzmann. Direct photons from relativistic heavy-ion collisions. *arXiv:hep-ph/0111114*, 2002.

[44] David Tlustý. Study of open charm production in p+p collisions at star. Dissertation thesis, Czech Technical University in Prague, 2014.

[45] Boris Tomasik and Urs Achim Wiedemann. Central and non-central hbt from ags to rhic. *arXiv preprint hep-ph/0210250*, 2002.

[46] CA Whitten Jr, Ahovi Kponou, Yousef Makdisi, and Anatoli Zelenski. The beam-beam counter: A local polarimeter at star. In *AIP Conference Proceedings*, volume 980, pages 390–396. AIP, 2008.

[47] Urs Achim Wiedemann and Ulrich Heinz. Particle interferometry for relativistic heavy-ion collisions. *Physics Reports*, 319(4):145–230, 1999.

[48] Urs Achim Wiedemann, Pierre Scotto, and Ulrich Heinz. Transverse momentum dependence of hanbury-brown–twiss correlation radii. *Physical Review C*, 53(2):918, 1996.

[49] Hanna Zbroszczyk. Studies of baryon-baryon correlations in relativistic nuclear collisions registered at the star experiment. Dissertation thesis, Warsaw University of Technology, 2008.